ORIGINAL ARTICLE

Linking horizontal crosshole GPR variability with root image information for maize crops

Lena Lärm[1] | **Felix Maximilian Bauer**[1] | **Jan van der Kruk**[1] |
Jan Vanderborght[1] | **Shehan Morandage**[2] | **Harry Vereecken**[1] |
Andrea Schnepf[1] | **Anja Klotzsche**[1]

[1]Agrosphere (IBG-3), Institute of Bio- and Geosciences, Forschungszentrum Jülich, Jülich, Germany

[2]Institute of Soil Science and Land Evaluation, University of Hohenheim, Stuttgart, Germany

Correspondence
Lena Lärm, Agrosphere (IBG-3), Institute of Bio- and Geosciences, Forschungszentrum Jülich, Jülich, Germany.
Email: l.laerm@fz-juelich.de

Assigned to Associate Editor Andrew Binley.

Abstract

Non-invasive imaging of processes within the soil–plant continuum, particularly root and soil water distributions, can help optimize agricultural practices such as irrigation and fertilization. In this study, in-situ time-lapse horizontal crosshole ground penetrating radar (GPR) measurements and root images were collected over three maize crop growing seasons at two minirhizotron facilities (Selhausen, Germany). Root development and GPR permittivity were monitored at six depths (0.1–1.2 m) for different treatments within two soil types. We processed these data in a new way that gave us the information of the "trend-corrected spatial permittivity deviation of vegetated field," allowing us to investigate whether the presence of roots increases the variability of GPR permittivity in the soil. This removed the main non-root-related influencing factors: static influences, such as soil heterogeneities and rhizotube deviations, and dynamic effects, such as seasonal moisture changes. This trend-corrected spatial permittivity deviation showed a clear increase during the growing season, which could be linked with a similar increase in root volume fraction. Additionally, the corresponding probability density functions of the permittivity variability were derived and cross-correlated with the root volume fraction, resulting in a coefficient of determination (R^2) above 0.5 for 23 out of 46 correlation pairs. Although both facilities had different soil types and compaction levels, they had similar numbers of good correlations. A possible explanation for the observed correlation is that the presence of roots causes a redistribution of soil water, and therefore an increase in soil water variability.

Abbreviations: BF, bare-field; EM, electromagnetic; EMI, electromagnetic induction; ERT, electrical resistivity tomography; GPR, ground penetrating radar; GS, growing season; MR, minirhizotron; PDF, probability density function; RLD, root length density; RV, root volume; RVF, root volume fraction; Rx, receiving antenna; sEIT, spectral electrical impedance tomography; SV, sensing volume; SWC, soil water content; Tx, transmitting antenna; VSI, Vienna scientific instruments; ZOP, zero-offset-profile.

1 | INTRODUCTION

The soil–plant continuum is influenced by multiple factors, including soil properties, soil nutrients, root system architecture, precipitation, irrigation, evapotranspiration, fertilization, and agricultural practices. Understanding how these factors interact in crops is beneficial to plant breeders for optimizing the belowground traits, achieving an optimal yield, efficiently using nutrients and water, as well as resistance to diseases. Both experimental and theoretical studies describe how plant roots can influence soil water variability and how they interact with soil heterogeneity. Spatial variability in crop roots (e.g., row crops) can also lead to soil water variability (Baroni et al., 2013; Hupet & Vanclooster, 2002). However, the presence of crop roots may decrease soil water variability since plants take up water from regions where water is present (Garré et al., 2011; Schlüter et al., 2013). Finally, crop roots and aboveground shoot may also increase variability in water infiltration and in this way impact soil water variability. Crops may funnel the rainfall that is intercepted by the canopy, thus creating local infiltration near the stem and roots. This can alter the soil structure and generate preferential infiltration paths so that more water is found in the presence of roots than without (Bui & Box, 1992; Hupet & Vanclooster, 2005).

Commonly used techniques to investigate the spatial and temporal distribution of roots and the soil water content (SWC) at the field scale mainly focus on investigating either root system architecture or soil properties. The in-situ exploration of the root system architecture can be achieved using labor-intensive and destructive methods such as excavation (Böhm, 1978; Weaver, 1926), shovelomics root crown phenotyping (Trachsel et al., 2010), auger sampling, and trench wall methods (e.g., do Rosário et al., 2000; van Noordwijk et al., 2001; Wasson et al., 2016). The main disadvantage of these destructive methods is the lack of repeatability. Non-invasive assessment could be used to optimize irrigation and fertilization and guide cultivar selection according to local soil conditions (Atkinson et al., 2019). A minimal-invasive alternative is provided by minirhizotron (MR) techniques, whereby transparent rhizotubes are permanently or temporarily installed within the soil, provide observation windows (e.g., Atkinson et al., 2019; Johnson et al., 2001; Rewald & Ephrath, 2013; Vamerali et al., 2011). These methods are less destructive, providing an option for the long-term monitoring of roots at the plot scale (e.g., Andrén et al., 1991; Cai et al., 2016; Svane et al., 2019; Vamerali et al., 2011). MR techniques enable the observation of both root distribution and root development during the vegetation period so that different crop growing seasons can be compared. However, MR facilities are expensive to install and maintain, and root observations are limited to 2D images that provide only a restricted display of the root system. Additionally, different installation techniques can disturb the soil and the rooting zone. This can cause soil smearing, loss of contact between soil and rhizotubes, and soil compaction, and the rhizotubes can act as obstacles for root growth (e.g., D. Guo et al., 2007; Johnson et al., 2001; Maeght et al., 2013; Rewald & Ephrath, 2013).

In the past decades, the field of non-invasive "agrogeophysics" has been established for in-situ investigation of root systems and the soil below agricultural crops (Garré et al., 2021). In agrogeophysics, methods such as electrical resistivity tomography (ERT), electromagnetic induction (EMI), and ground-penetrating radar (GPR) are often applied. ERT uses electrodes in the soil to image the electrical resistivity and has been shown to be well suited for in-situ monitoring of the soil–plant continuum and its structure, in particular soil water content and accordingly, soil water depletion patterns (Cassiani et al., 2016; Garré et al., 2012). Weigand and Kemna (2017, 2018) have successfully used spectral electrical impedance tomography (sEIT) to image crop root systems under controlled laboratory conditions, but it remains challenging to utilize these methods for in-field root phenotyping. Shanahan et al. (2015) identified a correlation in EMI-derived conductivity and SWC in root zones of wheat during soil water depletion dependent on the soil lithology. Additionally, Whalley et al. (2017) considered EMI, ERT, and penetrometer measurements to quantify differences in genotypic root activity from soil drying profiles of wheat. Under certain field conditions, such as drought, the resolution of the ERT method is not sufficient to monitor small-scale differences in soil water depletion for different crop genotypes (Cimpoiaşu et al., 2020). Further, the usage of fixed, permanently installed ERT lines can limit the monitoring area. EMI can map the apparent electrical conductivity of the soil by using an inductive signal; its lack of dependence upon a galvanic coupling with the soil results in a higher throughput compared to ERT. Both EMI and ERT can be used while crops are still growing (e.g., Blanchy, Watts, Ashton, et al., 2020; Blanchy, Watts, Richards, et al., 2020; Schmäck et al., 2021; Shanahan et al., 2015; Whalley et al., 2017). For a detailed review on EMI and ERT, refer to Ehosioke et al. (2020) and Cimpoiaşu et al. (2020). When investigating the soli-plant continuum, each of

---

Core Ideas

- Analiying spatial and temporal belowground GPR signal variability and root images for maize crop roots.
- Root images and GPR data show differences for different treatments.
- Linking of root volume fraction and GPR permittivity variability.

these methods has benefits but also limitations. The EMI and ERT signals are influenced by the electrical conductivity of the soil, which is controlled by the porosity, density, clay content, pore water saturation, temperature, and salinity of the pore water. Hence, deriving the SWC from these methods may be challenging. Furthermore, while EMI is a high-throughput method, allowing large areas to be mapped in a short amount of time, it lacks spatial resolution. Several studies indicate the potential of monitoring root water uptake or soil water distribution. However, the signal is influenced by multiple factors, and the spatial resolution is limited.

GPR is a geophysical method that can provide both high levels of spatial resolution and a direct link to SWC (e.g., Klotzsche et al., 2018), making it an ideal tool to monitor SWC as affected by root water uptake. GPR uses electromagnetic wave (EM) propagation in the soil (Jol, 2009) from which one can derive the relative dielectric permittivity (ε_r), and the attenuation of the EM wave can be linked to the electrical conductivity σ when using full-waveform inversion approaches (Klotzsche, Vereecken, et al., 2019). GPR typically uses high frequencies (50 MHz–3.6 GHz). The depth of penetration depends on the frequency of the antennae, as well as the attenuation of the EM wave, which is related to the electrical conductivity of the soil. This creates a trade-off between spatial resolution and the depth of penetration. The GPR-derived permittivity can be linked directly to SWC by using appropriate empirical or petrophysical relationships (e.g., Huisman et al., 2003; Steelman & Endres, 2011). The contrast in ε_r for different soil components (e.g., dry sand $\varepsilon_s = 6$, air $\varepsilon_a = 1$, and water $\varepsilon_w = 80$ [20˚C]) enables the establishment of a link between the ε_r and SWC. Note that depending on the frequency of the antennae and the applied petrophysical relationships, uncertainties can be present in the GPR-derived SWCs. GPR techniques can be divided into two major groups: surface and crosshole GPR. For surface GPR, the EM wave velocity and therefore the ε_r can be derived from the direct ground EM wave or reflected EM waves (Jol, 2009). When using the reflected EM waves, the derivation of the SWC is dependent on what is known about the soil horizon thickness. In contrast, using crosshole GPR allows a direct link from the EM wave velocity to ε_r (for more details, see Klotzsche et al., 2018). In recent years, surface GPR has been used to investigate the soil–plant continuum with large root systems such as tree roots (reviewed in L. Guo et al., 2013 and Rodríguez-Robles et al., 2017) and shrub roots (e.g., Cui et al., 2021; Liu et al., 2020, 2019; Parsekian et al., 2012). Although some studies investigated the possibility of estimating agricultural root systems (Delgado et al., 2017; Klotzsche, Lärm, et al., 2019; Liu et al., 2017; Wijewardana & Galagedara, 2010; Galagedara et al., 2002, 2003), the detection and mapping of finer root systems found in crops are still challenging using surface GPR. Individual fine roots of <0.002 m can only be detected using a higher frequency GPR (1600 MHz antennae)

as shown by Parsekian et al. (2012) under laboratory conditions. However, high-frequency applications at the field scale are difficult because of the high attenuation of the EM waves and the accompanying reduced penetration depth. Note that for most research questions, it is more interesting, although also more challenging, to investigate the entire root system and its root system architecture rather than just consider individual fine roots. This becomes even more challenging to quantify the entire root system and the surrounding soil.

Klotzsche, Lärm, et al. (2019) used time-lapse horizontal borehole GPR data to investigate the link between SWC, atmospheric conditions, soil, and crop types over several crop growing seasons. The authors showed that wheat and maize crops have different effects on the GPR signal and hence the SWC distribution. Individual maize crop rows were shown to have a clear impact on the SWC distribution, with a higher SWC below the maize rows in dry soil conditions. Regardless of the findings linking the atmospheric conditions and soil types to SWC distribution over time in the subsurface, open questions remained such as the effect of the roots and crops themselves on the obtained SWC along the horizontal rhizotubes. However, the influence of the wheat root system on the GPR signal could not be identified and hence the root systems of the individual crops and their direct effects on SWC were not estimated.

In this study, we provide multi crop growing season information about spatial variation in both soil water content and root observations. It shows the potential of GPR to noninvasively monitor and characterize the soil–plant continuum of maize crops by linking time-lapse horizontal crosshole GPR measurements and time-lapse root volume fractions derived from root images over the course of three crop growing seasons and within two soil types. Maize was used because of the larger crop row spacing, which provides a higher contrast between the root system and the soil compared to crops with narrow crop row spacing, such as wheat. Fine root systems are challenging, since GPR acquires information about a volume of soil which includes, for example, soil, water, roots, nutrients, fertilizer, microbes, and additionally applied agricultural management practices. The linking of time-lapse GPR measurements and root images obtained for three crop growing seasons allowed the investigation of whether the presence of roots influences the GPR permittivity. The calculation of the spatial permittivity deviation was done by subtracting the mean of the horizontal permittivity profile for each measurement date from the permittivity distribution. This was done to eliminate the effects due to the "dynamic" factors caused by different atmospheric conditions during the crop growing season. Blanchy, Watts, Richards, et al. (2020) used time-lapse EMI and ERT measurements to detect changes in electrical conductivity caused by cover crops, compaction, irrigation, and tillage. They subtracted a reference survey from the time-lapse surveys to remove

influences from the static effects, such as soil texture, and then analyzed the dynamic part of the electrical conductivity over time. Similar to this study, the "static" spatial permittivity deviations that were assumed to be caused by heterogeneities, for example, variability of soil properties, or artifacts, for example, unknown exact distances between emitting and receiver antennas, were subtracted from the spatial permittivity deviations of vegetated fields to obtain trend-corrected spatial permittivity deviations. The static spatial permittivity deviations were derived from spatial permittivity deviations measured in bare-field (BF) soil. These trend-corrected spatial permittivity deviations of the vegetated fields are a measure of the soil water or permittivity variability that is generated by the presence of roots. In this study, the key hypothesis is that spatial variation in root volume fraction can be linked with spatial variability in GPR permittivity. To test this hypothesis, we used repeated crosshole GPR measurements and root observations within minirhizotrons. First, the experimental setup is described, which is followed by a description of the root image measurement and data analysis. Next, the GPR measurements and processing steps are discussed. The time-lapse root data are then shown, followed by the time-lapse GPR data. Finally, a link between the RVF and GPR permittivity data variability is investigated.

2 | EXPERIMENTAL SETUP

2.1 | Minirhizotron facilities

Two MR facilities were present at the Selhausen test site within the TERENO (TERrestrial ENvironmental Observatories) Eifel-Lower Rhine observatory close to Selhausen (North Rhine-Westphalia, Germany) with the geographic coordinates 50°52'N, 6°27'E. They were geologically situated within fluvio-glacial sediments of the Rur River catchment (Bogena et al., 2018). Various studies have investigated the Selhausen test site using geophysical measurement techniques (e.g., Bauer et al., 2011; Brogi et al., 2019; Jadoon et al., 2012; Weihermüller et al., 2007).

At the Selhausen test site, different river deposits were present. The deposits could be observed due to a morphological slope of 4° from the upper terrace down to the lower terrace. Sediments at the upper terrace consisted of gravely, partly stony, and silty sand, whereas the lower terrace consisted of a silty, sandy, and slightly gravely loam with significant clay content, which gave the sediments of the lower terrace a firm consistency. The fluvio-glacial sediments were covered by a plow layer with a thickness of 20–30 cm for both terraces.

The MR facilities were situated on both the upper and lower terraces such that each MR facility was located in a river deposit where different soil properties were present (see Cai et al., 2016). The upper (R_{UT}) and lower (R_{LT}) MR facili-

ties each consisted of three plots (Figure 1a), which allowed the comparison of different agricultural treatments and different soil properties under the same atmospheric conditions. In each plot, three rhizotubes of 7- m length were installed at six different depths, between 0.1 and 1.2 m, below the surface. Rhizotubes were laid parallel to one another with a horizontal distance of 0.75 m. It is important to note that the depths of the rhizotubes varied between the individual crop growing seasons due to soil erosion and soil compaction after tillage and seedbed preparation (depths were measured every season). One end of each rhizotube was present in an access trench from which the measurements were performed. In the lower facility, R_{LT}, tubes were installed in horizontally drilled boreholes, and deviations could be up to 0.10 m. Because of the high stone content at R_{UT}, drilling horizontal boreholes was not possible (Cai et al., 2016). Instead, the soil was excavated in layers and refilled during the installation of the rhizotubes. The deviations in horizontal distance between R_{UT} rhizotubes were less than 0.02 m. Additionally, in order to make the measurements within the rhizotubes, various sensors were installed within the soil to measure the soil water potential (tensiometers and MPS-2 sensors manufactured by UMA GmbH and Decagon Devices, Inc., respectively), soil water content (time domain reflectometer in-house production), and soil temperature (MPS-2 sensors). Above ground at R_{LT}, there was a monitoring system for sEIT installed 3.5 m away from the trench (Weigand et al., 2022).

The MR facilities provided ideal circumstances to study the different components of the soil–plant continuum under field conditions and included data from different above- and belowground measurement techniques, for example, semi-4D geophysical data and information from root images. The belowground data acquired within the MR facilities between 2016 and 2021 can be found in Lärm et al. (2023). The belowground geophysical measurements were analyzed by Cai et al. (2016), Klotzsche, Lärm, et al. (2019), Yu et al. (2020, 2021), and Weigand et al. (2022). Other soil and root measurements were analyzed by Cai et al. (2017, 2018) and Morandage et al. (2021). Aboveground crop measurements are described by Nguyen et al. (2022).

2.2 | Experiment design and agricultural practices

In the time since the MR facility was installed, different wheat and maize cultivars have been sown for various crop growing seasons (e.g., Klotzsche, Lärm, et al., 2019; Morandage et al., 2021). Agricultural treatments, such as sowing density, sowing date, crop cultivars, and surface water treatment (sheltered, natural, and irrigated) vary for the different crop growing seasons. This study considered three seasons (2017, 2018, and 2020) in which maize (*Zea mays*) was sown. Different agricultural practices, which included irrigation, sowing
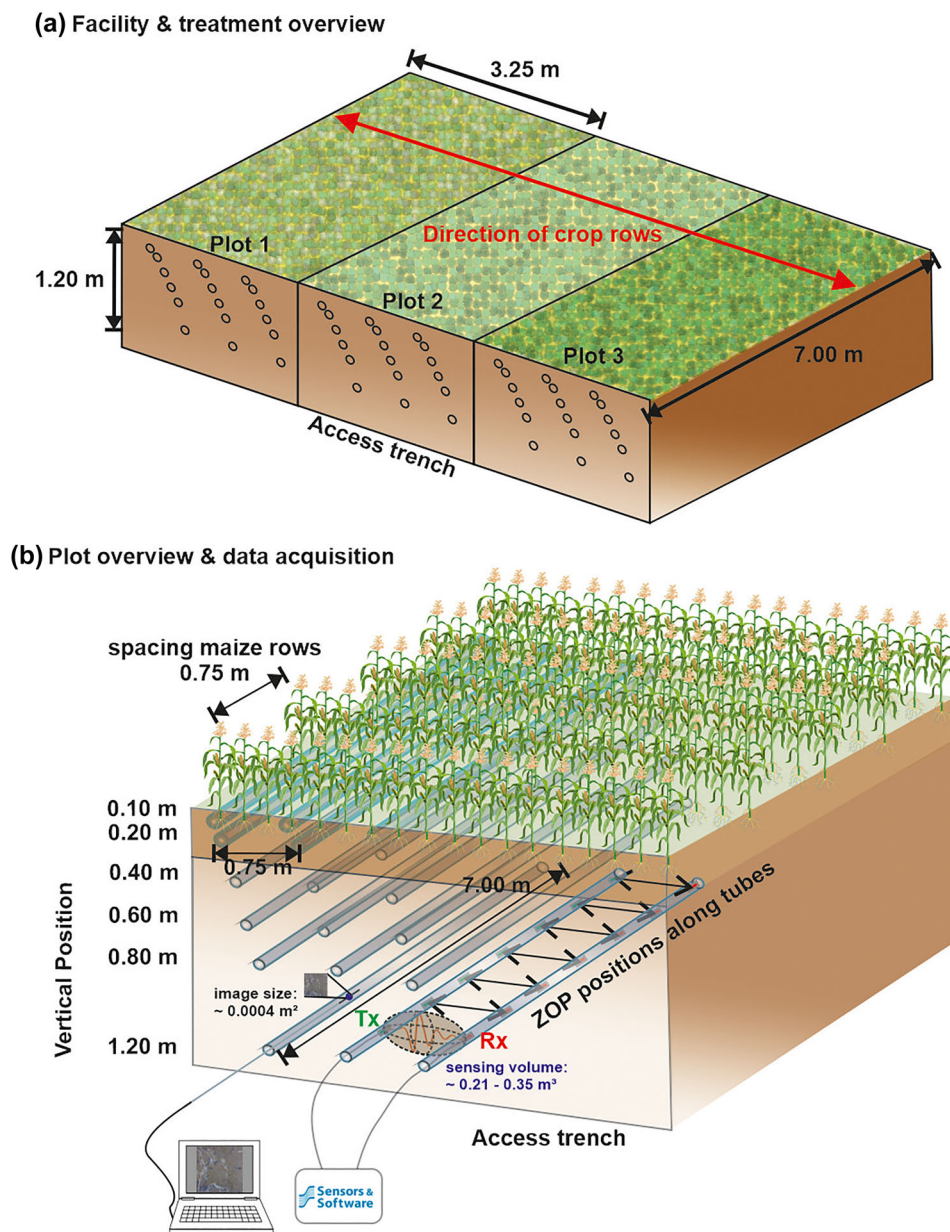
(a) Facility & treatment overview

3.25 m

Plot 1

1.20 m

Direction of crop rows

Plot 2

Plot 3

7.00 m

Access trench

(b) Plot overview & data acquisition

spacing maize rows
0.75 m

0.10 m
0.20 m
0.40 m
0.75 m
0.60 m
0.80 m

7.00 m

ZOP positions along tubes

image size:
~ 0.0004 m²

Tx

Rx

1.20 m

Vertical Position

sensing volume:
~ 0.21 - 0.35 m³

Access trench

Sensors &
Software

FIGURE 1 (a) Overview of the minirhizotron (MR) facilities. At each of the plots, different agricultural treatments were applied for the different crop growing seasons. The direction of the crop rows was perpendicular to the direction of the rhizotrubes (red arrow). The measurements were carried out within an access trench. (b) Overview of one representative plot within the MR facilities with the horizontal crosshole ground-penetrating radar (GPR) zero-offset-profiles (ZOP) measurement setup. Transmitter and receiver antennae are labeled Tx and Rx, respectively. Root images were acquired using a camera system attached to an index handle.

density, and varying cultivars, were simultaneously carried out for both MR facilities (overview in Table 1). For the crop growing seasons 2017 and 2018, the cultivar Zoey was sown on all three plots. A different sowing date (R_{UT}) and sowing density (R_{LT}) were chosen for Plot 1 in 2018. For the 2020 crop growing season, two different cultivars, Stacey and Sunshinos, were planted on the outer plots (Plots 1 and 3), respectively. For Plot 2, a mixture of the two cultivars with alternating rows was sown. The spacing between the individual maize crop rows was 0.75 m. When a higher sowing

density was applied, crop row spacing was kept constant, and the interrow distance was decreased. During the 2017 and 2018 growing seasons, an irrigation treatment was applied. While Plots 1 and 2 were rain-fed, Plot 3 was irrigated on a regular basis throughout the growing seasons. During the 2018 crop growing season, crops on Plots 1 and 2 showed severe stress symptoms, and emergency irrigation was necessary on a few occasions to ensure the continuation of the experiment. For the 2020 growing season, additional irrigation due to stress conditions was carried out equally on all

TABLE 1 Overview of the crop growing seasons used in this study, including the different agricultural practices, the maize growing stages, and number of measurement days.

Property	Year MR Facility	2017 R_{UT}	2017 R_{LT}	2018 R_{UT}	2018 R_{LT}	2020 R_{UT}
Treatment	Plot 1	Rain-fed	Rain-fed	Rain-fed	Rain-fed	Irrigated
	Plot 2	Rain-fed	Rain-fed	Rain-fed	Rain-fed	Irrigated
	Plot 3	Irrigated	Irrigated	Irrigated	Irrigated	Irrigated
Cultivar	Plot 1					Zea mays L. Sunshinos
	Plot 2	Zea mays L. 'Zoey'		Zea mays L. 'Zoey'		Mixture
	Plot 3					Zea mays L. Stacey
Sowing density (plants/m²)	Plot 1				16	
	Plot 2	10.66		10.66		10
	Plot 3				10.66	
Sowing	Plot 1		22.05.2018			
	Plot 2	04.05.2017		08.05.2018		29.04.2020
	Plot 3		08.05.2018			
Emergence	Plot 1		26.05.2018			
	Plot 2	09.05.2017		13.05.2018		12.05.2020
	Plot 3		14.05.2018			
Tasseling	Plot 1		21.07.2018			
	Plot 2	09.07.2017		09.07.2018		12.07.2020
	Plot 3		10.07.2018			
Silking	Plot 1		23.07.2018			
	Plot 2	14.07.2017		11.07.2018		15.07.2020
	Plot 3		12.07.2018			
Harvest	Plot 1		02.09.2018			
	Plot 2	12.09.2017		22.08.2018		23.09.2020
	Plot 3		22.08.2018			
Number of GPR meas.		22	21	22	19	9
Number of Root Images meas.		9	9	7	6	2

Abbreviations: GPR, ground-penetrating radar; MR, minirhizotron; meas., measurement.

three plots. The individual irrigation volumes can be found in Tables S1 and S2. Additionally, Table 1 provides information about the sowing, harvest dates, the dates for the different maize vegetation stages, and measurement times. Prior to the maize crop growing seasons, winter wheat had been sown at the MR facilities. The last winter wheat crops were harvested on July 26, 2016 (Klotzsche, Lärm, et al., 2019), with the soil laying fallow for 9.5 months without crop cover. Due to changes in project funding, in 2019, a flower meadow was planted but not further investigated.

3 | ROOT IMAGE ACQUISITION AND PROCESSING

The root images were obtained within the rhizotubes using a digital camera on an aluminum index handle (see Figure 2b).

Two different camera systems were used. For the 2017 dataset, the Bartz system (Bartz Technology Corporation) was used, and for the 2018 and 2020 datasets, the VSI system was used (Vienna Scientific Instruments GmbH). Due to time constraints, images were taken only at certain locations along the rhizotubes. The images taken from one rhizotube were composed of four groups of five images. The between-group spacing was 0.93 m (Figure 2a), and the within-group spacing varied between 0.08 and 0.12 m. For the time-lapse dataset, 40 images were captured from each rhizotube. This consisted of 20 images at an angle of 80° from the left side and 20 at an angle of 80° from the right side (Figure 2b). For comparison, the GPR-ZOP spatial measurement range is indicated in Figure 2a. In addition to the time-lapse root images, which were obtained over the three growing seasons 2017, 2018, and 2020, a continuous root image dataset was collected during the 2020 growing season. This dataset
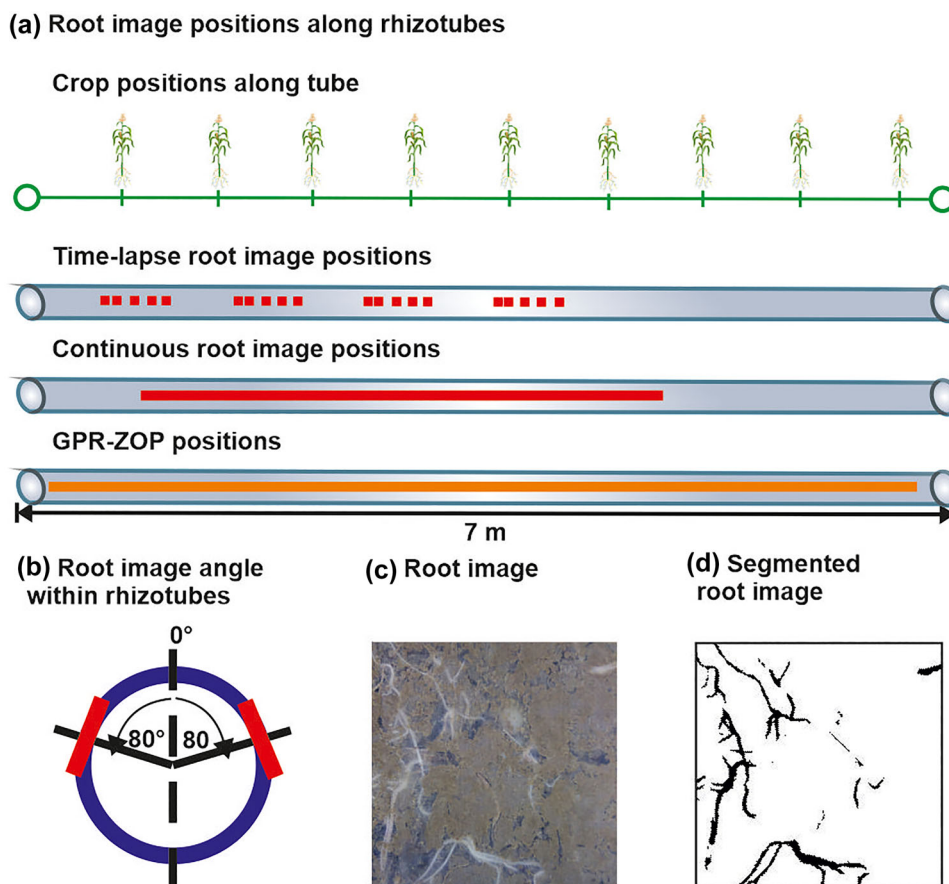
(a) Root image positions along rhizotubes

Crop positions along tube

Time-lapse root image positions

Continuous root image positions

GPR-ZOP positions

7 m

(b) Root image angle within rhizotubes

0°

80° | 80

(c) Root image

(d) Segmented root image

F I G U R E 2 (a) Root image locations within rhizotubes, with the location of the aboveground crop rows in comparison to the image locations. The upper rhizotube illustrates the positions of the time-lapse root images, the middle rhizotube illustrates the positions of the high spatially resolute root image measurement in 2020, the lower rhizotube illustrates the section where the ground-penetrating radar (GPR) zero-offset-profiles (ZOP) measurements were acquired. (b) Root image angles within the rhizotubes, (c) representative root image, (d) corresponding segmented root image after an automatic image analysis pipeline, developed by Bauer et al. (2022).

consisted of continuous sequences of root images over a length of 4 m in the rhizotubes (see Figure 2a). These measurements required approximately sevenfold more time than the regular root image measurements.

The root image dataset acquired over the 2017 crop growing season was briefly discussed in Morandage et al. (2021). For this study, the automatic image analysis pipeline developed by Bauer et al. (2022) was used to derive information from the root images (Figure 2c). The pipeline consists of the following processing steps. (i) Pre-processing of the images, which includes renaming, distortion correction, cropping, and resizing. While resizing, the dimensions of the images were changed to 0.0165 by 0.0235 m and 0.02 by 0.02 m for the Bartz and VSI camera systems, respectively, resulting in a root image size of ∼0.0004 m^2 and adds up to an area of ∼0.016 m^2 per rhizotube. For the continuous root image over 4 m, the image sizes of 0.02 by 0.02 m were made every 0.02 m, covering an image area of 0.16 m^2. (ii) Applying an automated image segmentation using RootPainter (Smith

et al., 2022), performed by a pre-trained neural network model; and (iii) converting the segmented images to binary images (Figure 2c), from which the root traits were extracted by RhizoVision Explorer (Seethepalli et al., 2021) for each individual root image.

The root volume per image was calculated by RhizoVision Explorer using the root length and the root diameter. To compare the root traits with the GPR measurements, the root volume fraction (%) (RVF) was used. This was defined as the volume percentage of space occupied by the roots in a respective soil volume. The respective soil volume was derived by assuming that the roots visible in the image were displaced by the rhizotube and would have otherwise grown within a volume that was equal to the image area times the outer rhizotube radius $r_{rhizotube}$ (0.032 m) (see Equation 2) (e.g., Cai et al., 2017; Morandage et al., 2021). This resulted in a sensing volume (SV) of 1.24×10^{-5} m^3 and 1.28×10^{-5} m^3 per image for the Bartz and VSI camera systems, respectively. Accordingly, the RVF was calculated by using the RV and the respective

TABLE 2 Comparison of the root volume fraction (RVF) and the root length density (RLD) as minimum, maximum and mean for R_{UT} and R_{LT} in 2017, respectively.

Property	R_{UT}		R_{LT}	
	RVF (%)	RLD (cm/cm³)	RVF (%)	RLD (cm/cm³)
Minimum	0.0000005	0.0006	0.000001	0.001
Maximum	0.36	1.84	0.75	2.1
Mean	0.01	0.103	0.042	0.25

Abbreviations: RLD, root length density; RVF, root volume fraction.

soil volume V_{soil}:

$$RVF = \frac{RV}{V_{soil}}, \qquad (1)$$

while using

$$V_{soil} = L \cdot W \cdot r_{rhizotube}, \qquad (2)$$

where L is the length of the image, and W is the width of the image. To compare the RVF data with the GPR measurements and taking into consideration the different V_{soil} of the methods, the mean RVF of four root image windows per position along the rhizotubes was used. This refers to images on either side of the two neighboring rhizotubes, from where the transmitting antenna (Tx) and receiver antenna (Rx) are inserted. Using four root images increases the image area to 0.001551 m² for each position along the rhizotube for the Bartz system and to 0.0016 m² for the VSI camera system. Note that images in both directions were used and not only in the GPR measurement direction to account for the scale difference between the size of the root images and the SV of the GPR measurements. The root length density (RLD) was also calculated for 2017, as it is a common parameter in rhizosphere science, and an overview in comparison with the RVF can be found in Table 2. The values for the years 2018 and 2020 can be found in the Tables S3 and S4.

In 2017, photographs were taken at different crop growth stages until the crops reached the reproductive stage to illustrate crop development at both facilities. A description of the individual growth stages is included in Figure 3. From this, the growth stages of the crops both above ground and below ground can be recognized. For Plot 3 in R_{UT}, an increased height of about 20 cm can be observed in Figure 3a for June 29, 2017, shown behind the line indicated by the two red arrows. Overall, the crops at R_{LT} performed visibly better than at R_{UT}. A similar trend can be seen in the root images for July 27, 2017 (Figure 3c). While a greater number of thicker roots are visible for deeper positions in R_{LT}, the roots in R_{UT} are thinner and less distributed in the deeper soil. Hanway (1966) described that the optimal development of maize is only dependent on nutrient uptake after the dough stage (reproductive stage 4), meaning that at this point maize crops
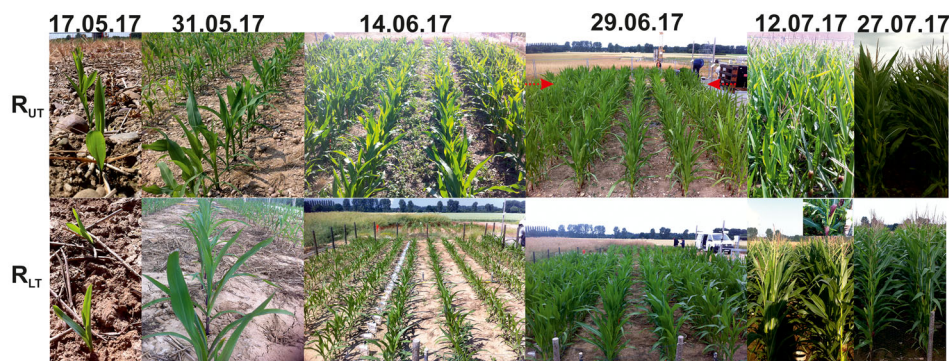
are expected to require less water. Previous to this stage, the development of the yield (number, size, and weight of the maize ears) is highly dependent on both the soil water and nutrient availability.

4 | GPR MEASUREMENTS AND DATA PROCESSING

During the three growing seasons under study, weekly time-lapse GPR measurements and discontinuous time-lapse root images were acquired. The time-lapse GPR data were acquired using the crosshole zero-offset-profiling (ZOP) measurement technique, employing a 200-MHz PulseEKKO borehole system manufactured by Sensors & Software. For ZOP measurements, Tx and Rx were located within adjacent rhizotubes (see Figure 1b). Tx emitted an EM wave through the soil, and the signal was recorded by Rx. Tx and Rx were moved in simultaneously in 0.05-m increments over the length of the rhizotubes. For time-zero calibration of the crosshole GPR data, wide-angle reflection and refraction measurements in the air were performed within the access trench. In this procedure, Tx was fixed, and Rx moved in 0.1-m increments over the 6-m distance. In total, over all three growing seasons, 53 datasets were obtained for R_{UT} and 40 for R_{LT}. For each measurement day, the permittivity values of the GPR measurements were estimated every 0.05 m along 5 m of the horizontal borehole length, resulting in 100 GPR traces per measurement depth. Only data between 2.5 and 6 m were considered because GPR data from close to the access trench where the soil sensors were located were not reliable and were therefore excluded. The 1.2-m depth in Plot 3 of R_{LT} was not measured due to a broken rhizotube, and a data gap is present between 2.8 and 3.3 m along the rhizotubes at 0.2-m depth due to the installed sEIT line (Weigand et al., 2022), which affected the GPR measurements.

To estimate the relative dielectric permittivity (ε_r) from horizontal GPR crosshole ZOP measurements, several processing steps are required: (i) apply a dewow filter, (ii) correct for time-zero, and (iii) estimate the first signal breaks (for more details, see Klotzsche, Lärm, et al., 2019). After finalizing these steps, picked travel times of the EM wave between

(a) Crop images - growing season 2017

(b) Vegetative stages of maize

	Vegetative (V) Stages						Reproductive (R) Stages		
	VE	V1	V3	V6	V9	VT	R1	R2 - R5	R6
Growing Stage	Emergence	First Leaf	Third Leaf	Sixth Leaf	Ninth Leaf	Tasseling	Silking	R2 - Blister R3 - Milk R4 - Dough R5 - Dent	Maturity
Days after Emergence (after Hanway, et al., (1966))		7	12	21	30	56	66	R2 - 78 R3 - 92 R4 - 102 R5 - 114	130
Date in 2017	09.05	16.05		31.05	07.06	09.07	14.07	27.07 (R2)	16.09
Date in 2018	26.05* 14.05	02.06* 21.05	07.06* 26.05	16.06* 04.06	25.06* 13.06	21.07* 09.07	31.07* 19.07	12.08* (R2) 31.07 (R2)	03.10* 21.09
Date in 2020	12.05	19.05	24.05	02.06	11.06	07.07	17.07	29.07 (R2)	19.09

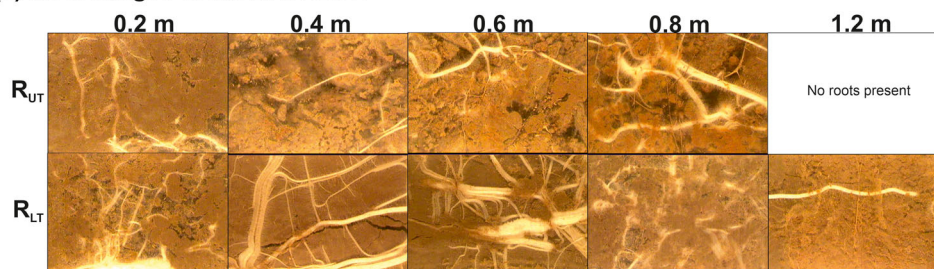**(c) Root images of the 27.07.2017**

FIGURE 3 (a) Images of both minirhizotron (MR) facilities during the 2017 crop growing season. (b) Overview of the maize vegetation stages and the corresponding dates for the crop growing seasons. (c) Root images of July 27, 2017 for different depths for both MR facilities. *For Plot 1 at R_{UT}, a later sowing date is applied. Hence, the respective dates for the different crop growing stages vary.

the adjacent rhizotubes were obtained for each ZOP position. Because of the known horizontal distance (0.75 m) between the rhizotubes, using the picked travel times allowed the calculation of the EM velocity for each ZOP position. Considering low-loss and non-magnetic soils (Jol, 2009), the EM velocity could be transformed into the relative dielectric permittivity ε_r of the bulk material with:

$$v = \frac{c}{\sqrt{\varepsilon_r}}, \tag{3}$$

where

$$\varepsilon_r = \frac{\varepsilon}{\varepsilon_0}, \qquad (4)$$

c is the speed of light ($\sim$0.3 m/ns), ε is the effective permittivity of the bulk material, and ε_0 is the permittivity of free space with 8.85×10^{-12} F/m. Note that from this point forward when permittivity is mentioned in the text, it refers to relative dielectric permittivity ε_r.

To obtain SWC from the relative permittivity, a petrophysical or empirical relationship is needed. One of the most common petrophysical volumetric mixing models is the complex refractive index model (Huisman et al., 2003). In this, it is assumed that the soil system consists of different phases, with different dielectric properties and volume fractions. The general formula for a system with n dielectric components is expressed by:

$$\varepsilon^\alpha = \sum_{i=1}^{n} \chi_i (\varepsilon_i)^\alpha, \qquad (5)$$

where ε^α is the bulk permittivity of the mixed system, and α is a fitting exponent, which accounts for the geometry of the system. χ_i and ε_i indicate the volume fraction and permittivity of the i-th component of the system, respectively. Commonly, three-phase soil systems are used, which include soil, water, and air. Using $\alpha = 0.5$ for the geometry factor and $\varepsilon_a = 1$ for the permittivity of air, Equation (5) can be reformulated for a three-phase system to:

$$\varepsilon_r = \left[(1-\phi) \cdot \sqrt{\varepsilon_s} + \theta \cdot \sqrt{\varepsilon_w} + (\phi-\theta) \right]^2, \qquad (6)$$

where ϕ is the soil porosity. ε_s and ε_w represent the permittivities of the soil (solid phase) and water components of the system, respectively. θ represents the volumetric SWC. Rearranging Equation (6), the SWC for the three-phase system could be calculated using:

$$\theta = \frac{\sqrt{\varepsilon_r} - (1-\phi)\sqrt{\varepsilon_s} - \phi}{\sqrt{\varepsilon_w} - 1}. \qquad (7)$$

Like Klotzsche, Lärm, et al. (2019), an $\varepsilon_w = 84$ at 10°C was used, which represents the mean soil temperature obtained from the soil temperature sensors. ε_s was 4.7 and 4.0 for the R_{UT} and R_{LT}, respectively.

The SV of the GPR data, described by the Frensel volume, is an elongated rotational ellipsoid where the foci are at the locations of Tx and Rx (see Figure 1). The size of the volume depends on the spacing between the antennae, center frequency, and the bulk permittivity of the soil. The SV for intermediate soil water content conditions for R_{UT} was approximately 0.35 m³ (see Klotzsche, Lärm, et al., 2019). Note that the SV for the GPR data was significantly larger

than the investigated soil volume to obtain the RVF values, such that a direct comparison was not possible. In addition, the GPR-derived permittivity values are influenced by the soil, the water content of the soil, and the water content of the roots. The separate contribution of each factor cannot be disentangled with this type of measurement setup. Since the RVF was very small (see Table 2) and the dielectric permittivity of the soil particles was small compared to that of water, the main contribution to the bulk soil permittivity came from the soil water (e.g., Cassidy, 2009). Additionally, uncertainties of the solid phase are higher for dry conditions with low saturation of the soil. Therefore, in the following, the obtained relative permittivity from the measured GPR signals and its spatial and temporal variability is discussed.

5 | SPATIAL AND TEMPORAL VARIABILITY OF THE SOIL–PLANT CONTINUUM

Root images and crosshole GPR data were acquired, when possible, on a weekly or biweekly basis over three crop growing seasons. The total number of measurements per crop growing season is shown in Table 1. For the GPR dataset, the information from the 0.1-m deep rhizotubes was excluded, mainly due to the interference of the critically refracted air wave with the direct wave. The GPR traces at a depth of 0.2 m also show an impact of this interference, particularly for dry conditions. However, the uncertainties remain within an acceptable range, and the data can still be used for further analysis (Klotzsche, Lärm, et al., 2019; Yu et al., 2021). Since the GPR has a larger SV than the root images, the data acquired from the root images at a depth of 0.1 m are included.

5.1 | Time-lapse root data

From the results of the automatic image analysis pipeline (Bauer et al., 2022), the RVF information was derived for each rhizotube for both MR facilities. For each plot, the mean RVF was calculated at each depth, taking into consideration both rhizotubes, which were also used for the GPR measurements. In some cases where unrealistic RVF values occurred due to changes in image settings and acquisition errors, data needed to be excluded.

The curves for the root development over time with the root arrival for 2017 are shown in Figure 4, where the RVF is plotted for all three plots for R_{UT} and R_{LT} as a function of time. Depths of 1.2 m were only measured late in the crop growing season, due to the absence of roots in the earlier vegetation stages. For most of the root arrival curves, an increase in RVF over time was observed, where a strong increase in RVF was mostly present around the date of tasseling and silking.
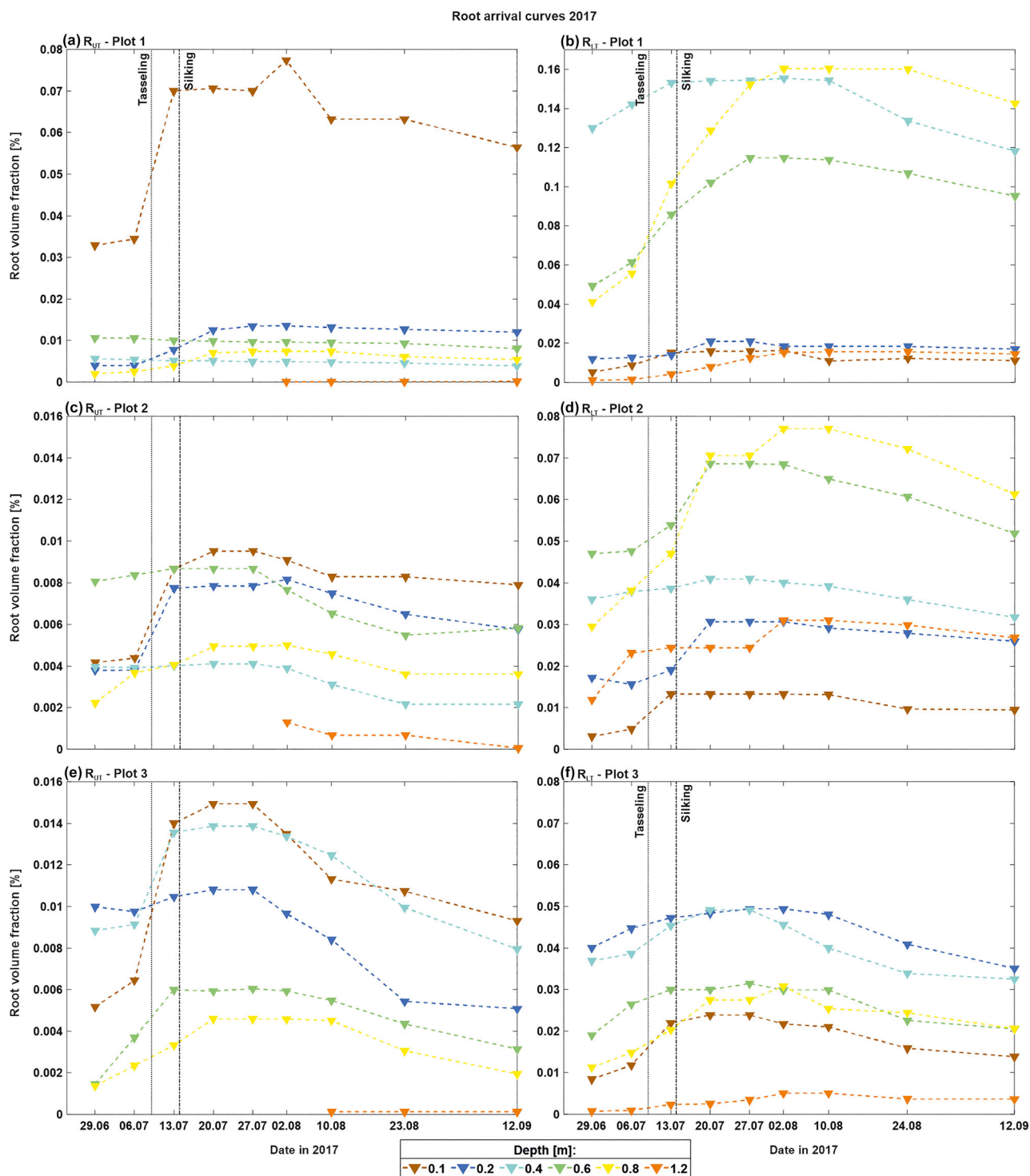
FIGURE 4 Root arrival curves in root volume fraction (RVF) for 2017 for the three plots for R_{UT} and R_{LT}, left and right, respectively. The root images were measured within the same rhizotubes where the ground-penetrating radar (GPR) antennae was placed. The colored triangles represent the RVF over time, which were median-filtered over 3 measurement days. The colors indicate the different depths. Tasseling and silking are indicated by the vertical lines. Note the different y-axes scales for Plot 1 in comparison to Plots 2 and 3.

During tasseling, the male flowers start to shed their pollen. This takes place when the plant has reached its full height. Silking is the emergence of silks from the ear shoot of the female maize flower. At the end of the crop growing season, up to the harvest date, there was a significant decrease in RVF. In general, R_{LT} showed higher RVF than R_{UT}. For R_{UT}, the maximum RVF was below ~0.08%, and for R_{LT}, the maximum RVF was ~0.15% (see Figure 4). In addition, there were considerable differences in root development at the different depths, both between the MR facilities and between individual plots. The highest RVF for both R_{LT} and R_{UT} were found in Plot 1 at 0.8 m and 0.1 m, respectively. The next highest RVF obtained in R_{UT} was at Plot 3, followed by Plot 2, and for R_{LT} Plot 2 followed by Plot 3. The maximum rooting depths for both MR facilities in the 2017 crop growing season and the results obtained using an additional excavation measurement showed similar results (see Klotzsche, Lärm, etal., 2019; Morandage et al., 2021). In these studies, a maximum rooting depth of 1 m for R_{UT} and of 1.40 m for R_{LT} was detected, which exceeded the maximum observation depth for R_{LT}. Figure 5 shows the same RVF data as Figure 4 but plotted as a function of depth, such that the depth distribution is both more clearly visible and not median-filtered over time. A comparison of the three individual plots of R_{UT} and R_{LT} reveals significant differences. The natural/rain-fed Plots 1 and 2 at R_{UT} had maximum values at a depth of 0.1 m and 0.6 m, although for Plot 1, the maximum value at a depth of 0.1 m was significantly larger than at a depth of 0.6 m. Note that the axis for the 0.1-m depth was significantly larger than the other depths. At R_{LT}, the natural/rain-fed Plot 1 showed two maxima in RVF at depths of 0.8 m and 0.4 m, whereas for Plot 2, a maximum was present only at a depth of 0.8 m. Note that the axis range for Plot 1 was again significantly larger than for Plots 2 and 3. The irrigated Plot 3 showed a local maximum in RVF at a depth of 0.4 m for R_{UT} and at depths of 0.1 m and 0.4 m for R_{LT}. The same analysis was carried out for 2018 and 2020, and the results can be found in Figures S1 and S3, respectively. The depth distribution of 2018 was similar to that of 2017, and what few differences were observed were possibly related to differences in measurement dates. A large difference was visible for R_{UT} Plot 3, where the highest values in RVF were present at depths of 0.4 m and 0.6 m. During the 2020 growing season, only two measurements at R_{UT} were possible, and therefore no comparison was made.

5.2 | Time-lapse GPR data

For each measurement day, the permittivity values of the GPR measurements were estimated for each position (every 0.05 m) along the horizontal rhizotubes for five depths and three plots/treatments. The obtained permittivity values were then plotted as horizontal permittivity profiles between the rhizotubes. Figure 6 shows semi-3D images for a 1.2-m-depth by 9-m-width by 3.5-m-length soil volume, obtained for April 26, 2017, and July 27, 2017, which show the horizontal permittivity profiles before and during the maize growing season.

Overall, the permittivity of R_{LT} indicated higher values than R_{UT}, which was related to the porosity ϕ and soil type differences of both MR facilities. While the topsoil of R_{UT} had an approximate porosity of $\phi = 0.33$ and the subsoil of $\phi = 0.25$, the topsoil and subsoil of R_{LT} had a porosity $\phi = 0.4$ and $\phi = 0.35$, respectively. Additionally, at R_{LT}, a shallower water table depth was present (seasonal fluctuations between 3 and 5 m below the surface, see Jadoon et al., 2012). Generally, the permittivity increased with increasing depth for R_{UT} and R_{LT}. Comparing the two measurement days, the permittivities before the growing season were generally slightly higher than during the season for both MR facilities, which was related to the weather conditions. To better understand the seasonal changes, the mean permittivity per depth over time was compared with the weather data (Figures 7 and 8 for R_{UT} and R_{LT}, respectively).

Similar to the findings from the root arrival curves and RVF depth distribution (Figures 4 and 5), there was a difference in permittivity between the individual plots. For R_{UT}, a permittivity gradient between the three plots was present (Figure 6a,b), with Plot 1 having the lowest permittivity values, followed by Plots 2 and 3. This was particularly evident before the growing season (see gray frames in Figure 7). The difference was particularly distinct at a depth of 0.2 m (plow layer), while the irrigated Plot 3 showed the highest permittivity values. Although Plots 1 and 2 received the same surface water treatment, Plot 1 showed lower permittivity values at all depths.

Additionally, it can be assumed that because of the larger SV of the GPR measurements, information acquired below a depth of 1.2 m included naturally deposited soil. Similar to R_{UT}, R_{LT} had a visible permittivity gradient between the individual plots, with Plot 1 showing the lowest permittivity values, and Plot 3 the highest (Figures 6 and 8b,d). Additionally, this gradient from lower to higher permittivity values was equally noticeable over all depths. In contrast to R_{UT}, the 0.2-m depth had the lowest permittivity values, compared to greater depths, and the permittivity increased with increasing depth. The horizontal permittivity variations were smaller compared to the vertical variation for both MR facilities (Figure 6c,f). The areas along the rhizotubes with higher permittivity values in depths of 0.2 m coincided with the spatial aboveground location of the maize crop rows, indicated by green diamonds (see also Klotzsche, Lärm, et al., 2019). These patterns were more distinct for R_{UT} than R_{LT}, caused by the higher permittivity changes for R_{UT}. Greater depths did not show these clear permittivity patterns, although there were variations along the rhizotube with smaller differences.
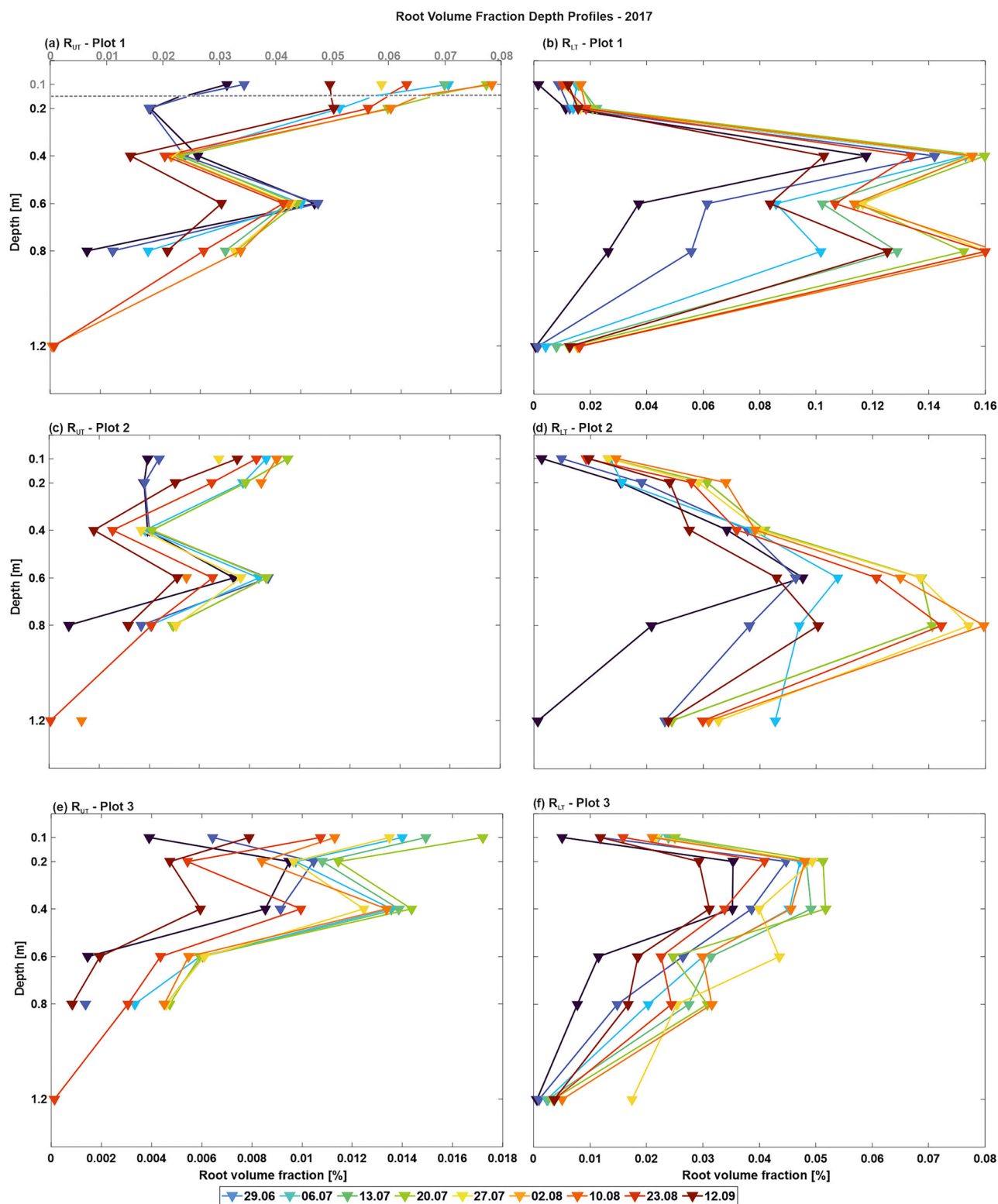
FIGURE 5 Root volume fraction (RVF) depth profiles of 2017 for R_{UT} (a), (c), and (e) and R_{LT} (b), (d), and (f). The colored triangles represent the RVF values for the different depths, where the different colors represent the measurement date over the crop growing season. Note the different x-axis for R_{UT} and R_{LT} below all plots and a separate axis for Plot 1 of R_{LT} and adepth 0.1 m of Plot 1 of R_{UT} shown on top of the figure.
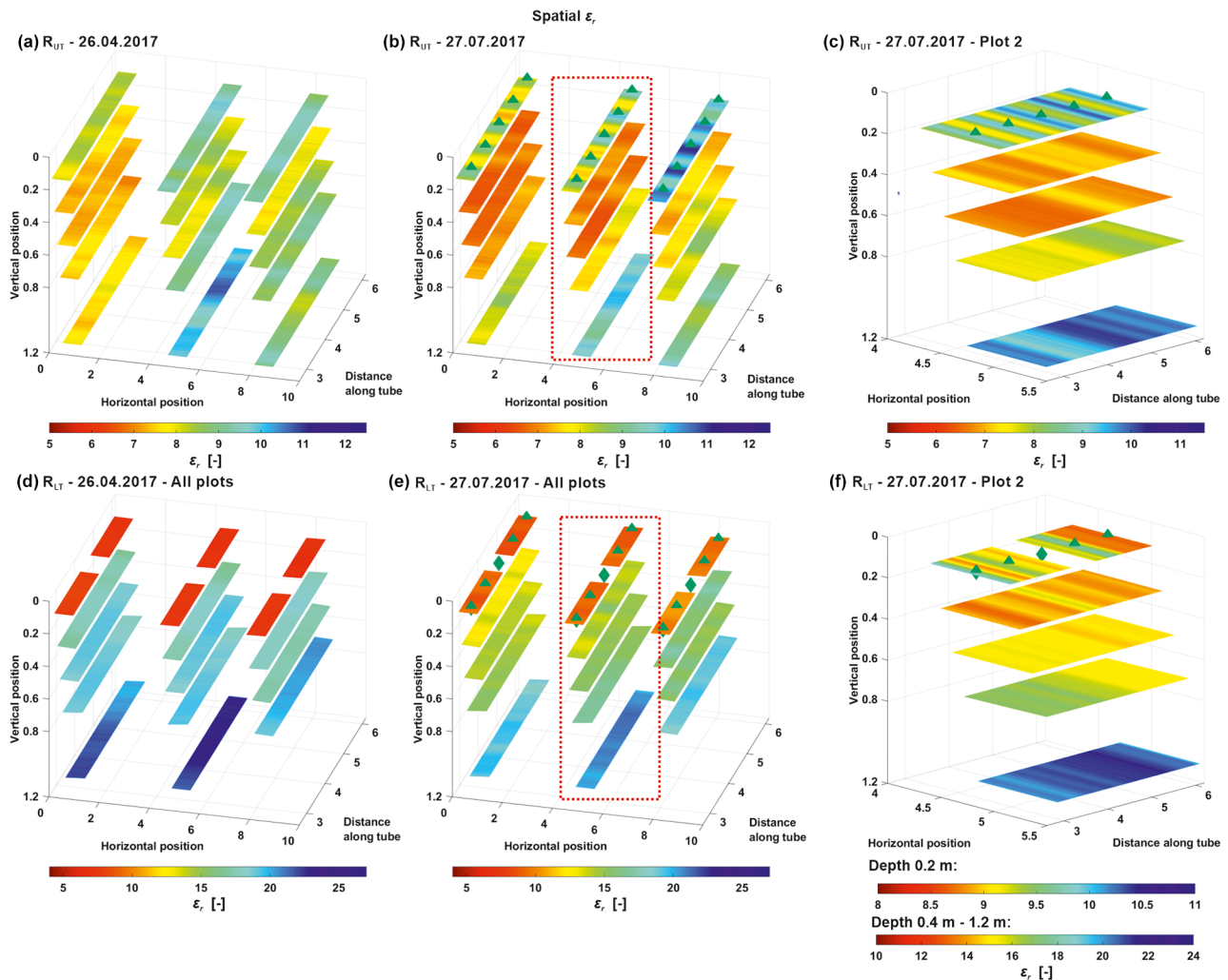
FIGURE 6 Semi-3D plots of horizontal permittivity profiles for 2 days during the crop growing season 2017. Permittivity results for R_{UT} and R_{LT} for the dates April 26, 2017, and July 27,2017, for (a) and (b) and (d) and (e), respectively. The different colors represent the permittivity values along the rhizotubes, the green diamonds indicate the aboveground location of the maize crop rows, and the red dashed rectangles indicate two zooms for Plots 2 shown in (c) and (f) with an adjusted color bar. Note that for April 26, 2017, no crops were sown, while for July 27,2017, maize crops were present.

The semi-3D plots of winter wheat in Klotzsche, Lärm, et al. (2019) did not show the same patterns within the horizontal permittivity profiles.

To investigate a possible link between permittivity variations and atmospheric changes, comparisons between the mean permittivity values per day and depth, and the daily precipitation and temperature for both MR facilities were made (Figures 7 and 8). Similar to the findings observed in Figure 6, it was found that along the rhizotubes the mean permittivity (i) was higher for R_{LT} than R_{UT}; (ii) mostly increased with increasing depth, except for at a depth of 0.2 m for R_{UT}, where the highest mean permittivity was observed during periods with high precipitation and irrigation events; and (iii) showed dependence on the weather conditions, where high permittivity values were observed during the periods of high precipitation/irrigation and lower temperatures. Presumably,

the responses to changes in the weather conditions were different due to the different soils of the MR facilities. While for R_{UT} there was a faster response of the mean permittivity at all depths, R_{LT} exhibited a delayed response with increasing depth. As previously mentioned, this was likely caused by the higher porosity of the fine-grained soil, and for R_{LT}, perhaps additionally due to the closer distance of the groundwater table and the associated capillary rise (see Klotzsche, Lärm, et al., 2019). Interestingly, for R_{LT}, a trend was observed that did not seem to correlate with the weather conditions. After the silking and tasseling, a steady decrease in mean permittivity at all depths was apparent, even in correlations with precipitation events when temperatures did not change. The lack of effects of precipitation events was likely because the increase in SWC was counteracted by an increased root water uptake. This effect was less recognizable for R_{UT}. The same
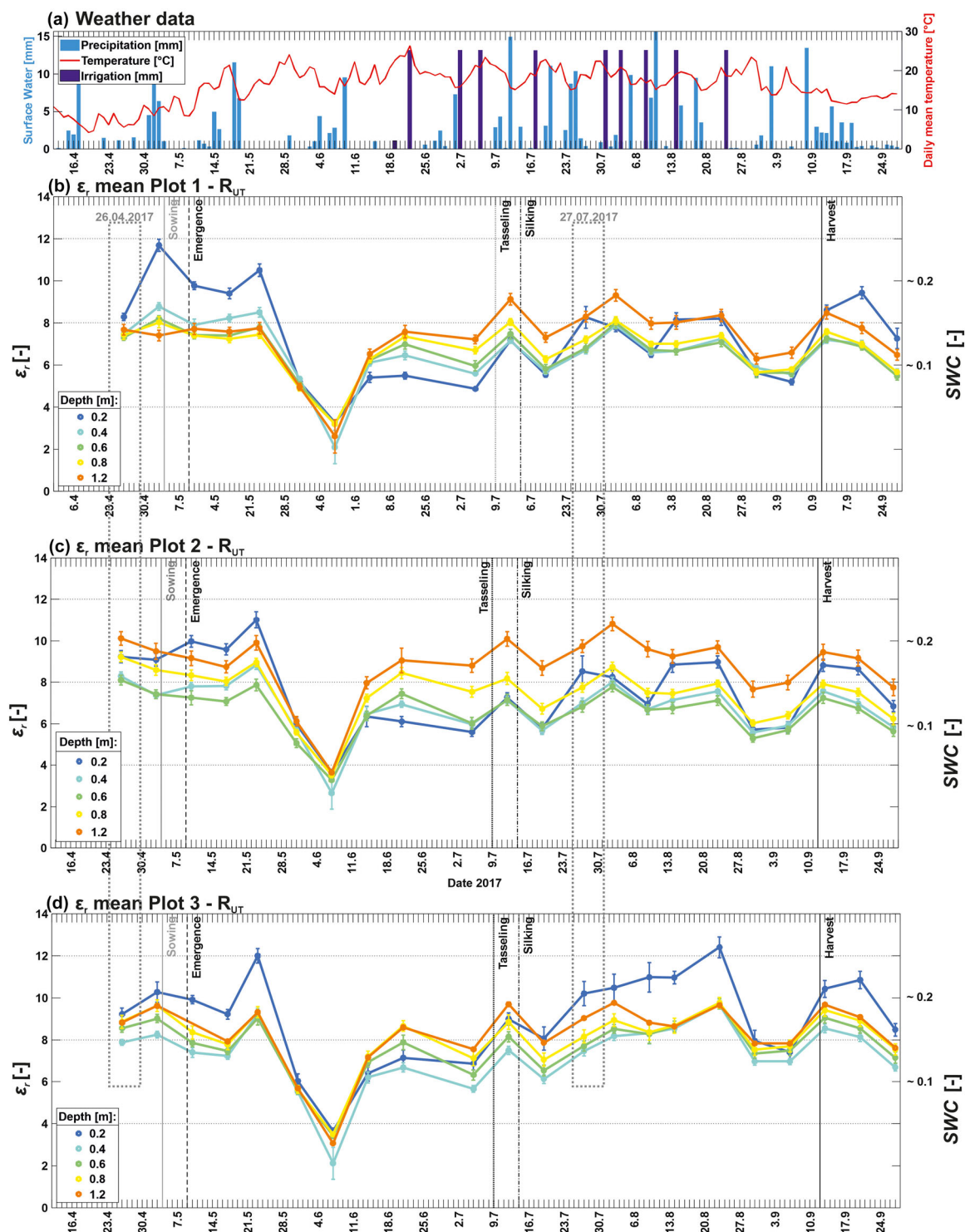
FIGURE 7 Comparison of the weather data and permittivity for R_{UT} during the 2017 crop growing season. (a) Weather data: the solid red line represents the daily temperature values, and the light blue bars represent the daily precipitation values. The dark blue irrigation values are only valid for Plot 3. Mean permittivity per depth for Plots 1–3 are shown in (b) and (d). The colored circles with the error bars indicate the permittivity mean along the rhizotube with its standard deviation as error bars. The colored solid lines connect the individual measurement days. The horizontal lines represent the dates for the vegetation stages and sowing and harvest dates. For convenience, the approximate soil water content (SWC) values were added on the right-hand axis for (b) and (d) using the three-phase complex refractive index model (CRIM).

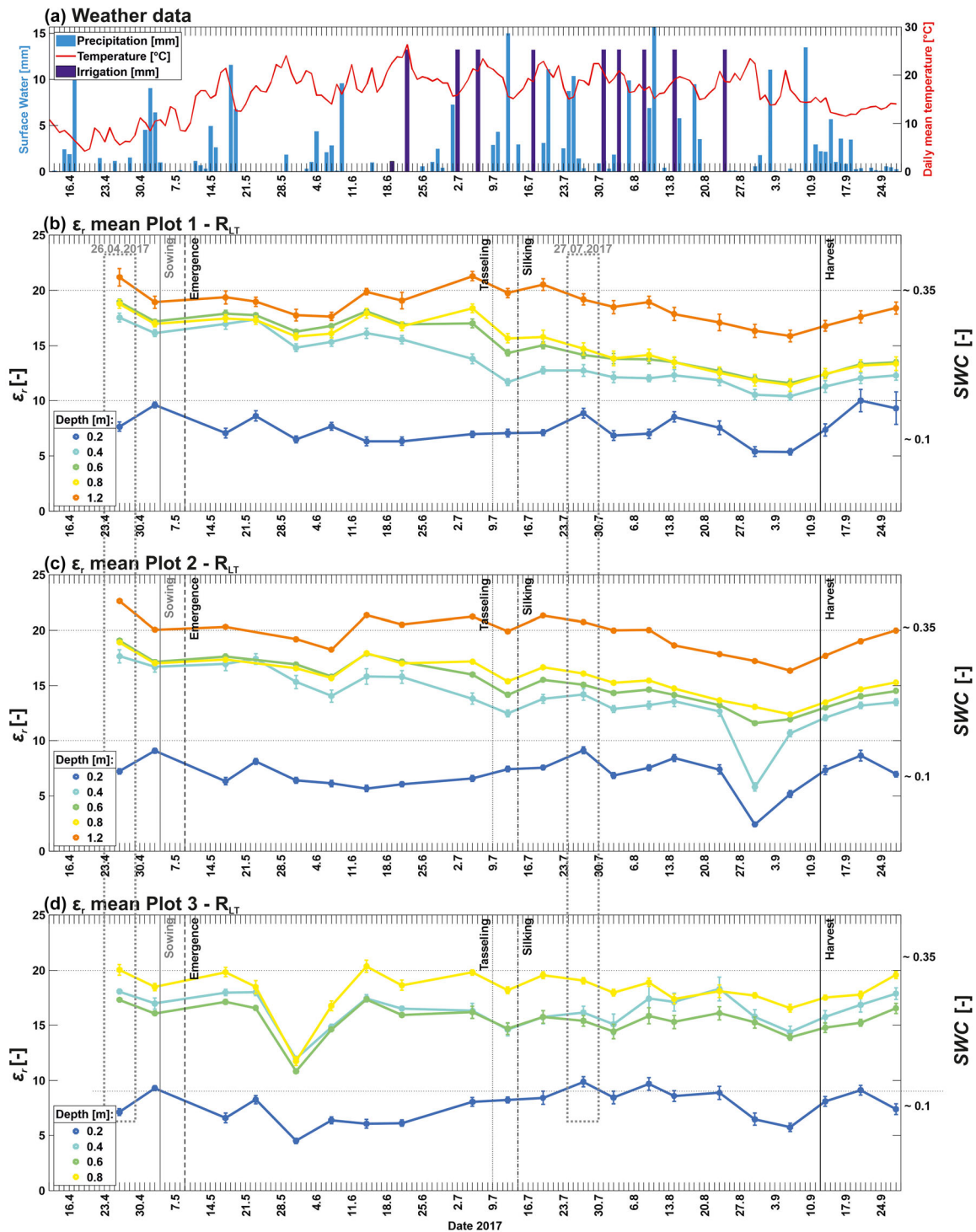**Temporal GPR data for different soils in comparison with the weather data**

FIGURE 8 Comparison of the weather data and permittivity for R_{LT} during the 2017 crop growing season. (a) Weather data: the solid red line represents the daily temperature values, and the light blue bars represent the daily precipitation values. The dark blue irrigation values are only valid for Plot 3. Mean permittivity per depth for Plots 1–3 are shown in (b) and (d). The colored circles with the error bars indicate the permittivity mean along the rhizotube with its standard deviation as error bars. The colored solid lines connect the individual measurement days. The horizontal lines represent the dates for the vegetation stages and sowing and harvest dates. For convenience, the approximate soil water content (SWC) values were added on the right-hand axis for (b) and (d) using the three-phase complex refractive index model (CRIM).

analysis was carried out for 2018 and 2020, and the results confirming these findings can be found in Figures S4 and S6, respectively.

6 | LINKING DEPTH-DEPENDENT RVF WITH DEPTH-DEPENDENT GPR PERMITTIVITY VARIABILITY

This section investigates the connection between the RVF and GPR permittivities. Although Plots 1 and 2 at R_{UT} and R_{LT} had the same surface water treatment in 2017 and 2018, the observed RVF depth profiles shown in Figures 4 and 5 and permittivities in Figures 6–8 obtained in 2017 showed distinct differences. The measured RVF and permittivity data from 2018 show significantly smaller differences, as shown in Figures S1–S3. A possible explanation for the larger differences between Plots 1 and 2 in R_{UT} and R_{LT} in 2017 than in 2018 is the application of different surface water treatments for Plots 1 and 2 from previous years. While Plot 2 was always under rain-fed conditions, Plot 1 was sheltered between 2012 and 2016 for R_{UT} and between 2014 and 2016 for R_{LT}. The rain-out shelter for Plot 1 resulted in drier soil and, consequently, both a different root distribution within the soil profile and lower crop growth compared to the other plots. This generated a so-called "memory effect." Consequently, the soil conditions at the beginning of the experiment were not the same for both years, resulting in different patterns in SWC and root growth.

The influence of the maize crops on the horizontal permittivity profiles is clearly shown in Figure 6c,f. Five crop rows were present along the rhizotubes, overlapping with the GPR measurements as shown in Figure 2, and five peaks could be identified in the permittivity values at the shallowest depth of 0.2 m. This indicated that increased SWC values were present between the two rhizotubes, probably due to the presence of shallow crown roots.

Since root images were collected only at selected locations, as indicated in Figure 2, no direct comparison could be made between the observed RVF and permittivity along the rhizotubes. Only once on August 5, 2020, a labor-intensive continuous image of the roots made along the complete rhizotubes was acquired. Figure 9 shows the results and includes the measured permittivity values. Additionally, five peaks in the permittivity can be observed at the 0.2-m depth, which correspond to the five maize rows, though they show a considerable shift. The permittivity peaks at 1.5 and 2.25 m along the rhizotubes also correlated with the corresponding root information (RVF). However, while multiple small peaks in RVF were present between 2.5 and 5 m, there was no clear direct correlation between the RVF and permittivity data. Although the SV of the RVF was limited to the area directly around the rhizotube and the GPR SV represented the larger soil vol-

ume in between two rhizotubes, these results indicate that the presence of roots increases the variability in permittivity. In contrast, permittivity in a BF, where no roots are present, showed a very small variation in permittivity (Figure 6). In the following section, it is assumed that the roots observed along the rhizotubes represented the root growth at that specific depth, and an investigation of whether a correlation exists between the average RVF along the rhizotubes and the variability in permittivity follows.

6.1 | Calculation of time-lapse variability analysis of GPR data

The investigation into the effects of the soil–plant continuum on the GPR-derived permittivity distinguished between static and dynamic influences. Static influences were soil heterogeneity and variations in the distances between rhizotubes and exerted a time-constant effect on the permittivity at the MR facilities. The dynamic influences were dominated by the temporal changes in permittivity caused by the seasonal variations in weather conditions (e.g., precipitation and evapotranspiration) as well as the soil water depletion caused by the root water uptake. To come up with a proxy for the permittivity changes related to the presence of roots, it was necessary to optimally reduce static effects and minimize the dynamic influences caused by atmospheric conditions for each measurement day.

When investigating the horizontal permittivity profiles over the course of the measurement season, it was observed that the vertical permittivity variations with depth for the different dates were caused by changes in the weather conditions (Figure 10a), as shown in the exemplary case for a depth of 0.8 m within Plot 2 of R_{LT}. To minimize the dynamic factors caused by different atmospheric conditions during the crop growing season, each day needed to be considered separately. As a first step, we reduced the dynamic influences for each horizontal permittivity profile:

$$\varepsilon_{r_{i,j}}{}' = \varepsilon_{r_{i,j}} - \overline{\varepsilon_{r_{i,\cdot}}} \tag{7}$$

by calculating the mean $\overline{\varepsilon_{r_{i,\cdot}}}$ along the rhizotubes for each horizontal permittivity profile, and then this value was subtracted from the $\varepsilon_{r_{i,j}}$ of the individual ZOP positions along the rhizotubes. Here, i and j indicate the date and the position along the rhizotube, respectively. These so-called spatial permittivity deviations $\varepsilon_{r_{i,j}}{}'$ represent the deviations of the individual permittivities at the individual ZOP positions j from the mean $\overline{\varepsilon_{r_{i,\cdot}}}$ along the horizontal permittivity profiles and are independent from the seasonal changes in SWC conditions. This step was repeated for each measurement day individually. Data from the growing season and the BF measurements, which were
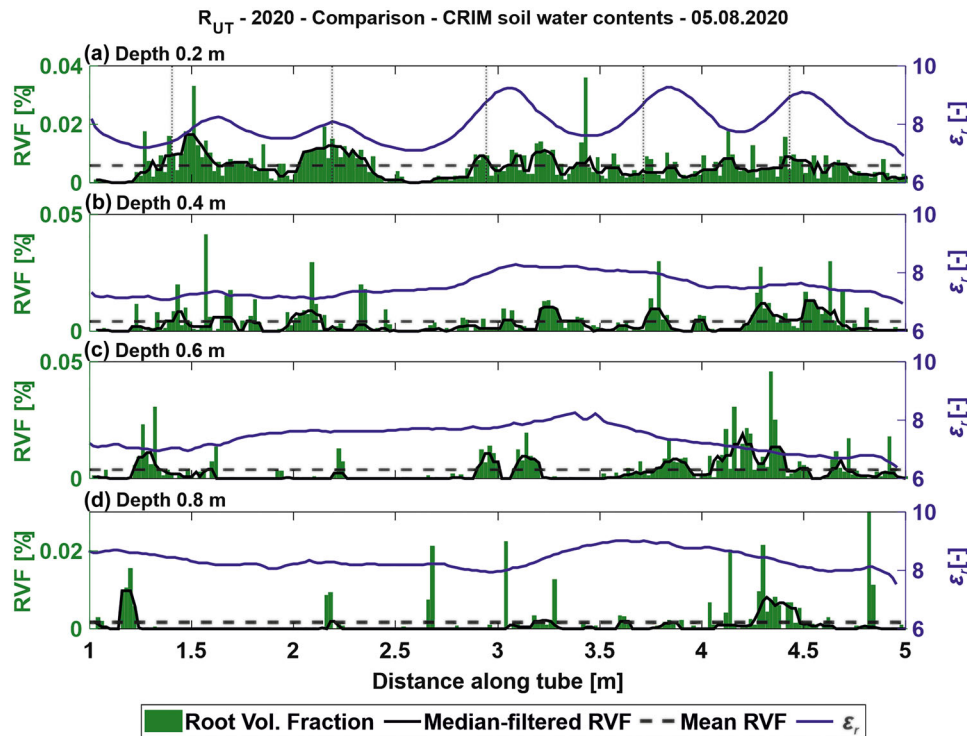
FIGURE 9 Comparison of the permittivity high-resolution root image dataset measured on August 5, 2020, and the respective root volume fraction (RVF). The different plots represent the different depths of 0.2–0.8 m, (a)–(d), respectively, for Plot 2 at R_{UT}. The solid blue line indicates the permittivity. The green bars indicate the RVF along the rhizotubes. The black solid line indicates the smoothed RVF along the rhizotube over five positions. The dashed black line represents the mean RVF along the rhizotubes.

collected before the sowing of the maize crops, were considered separately. Comparing the derived spatial permittivity deviations $\varepsilon_{r_{i,j}}{}'$ for all measurement dates in Figure 10b,c, a trend of reoccurring patterns is observed. The obtained spatial permittivity deviations for the BF measurements shown in Figure 10c have a much smoother and more regular trend than the measurements from the growing season. The mean BF spatial permittivity deviations $\overline{\varepsilon_r^{BF}{}_{\cdot,j}{}'}$ were calculated for each season separately and for all positions along the rhizotube j, since small changes were present between the individual $\overline{\varepsilon_r^{BF}{}_{\cdot,j}{}'}$ values for each year. All daily spatial permittivity deviations for the BF $\overline{\varepsilon_r^{BF}{}_{i,\cdot}{}'}$ can be found in Figure A1 for 2017 and 2018. Additionally, the $\varepsilon_r^{BF}{}_{i,j}{}'$ values for R_{UT} can be found in Figure S7. As a final step, the trend-corrected spatial permittivity deviations $\Delta \varepsilon_{r_{i,j}}{}'$ were derived for each growing season measurement along the horizontal permittivity profiles. Static effects were removed by subtracting $\overline{\varepsilon_r^{BF}{}_{\cdot,j}{}'}$ from the daily variability during the crop growing season (GS), represented by $\varepsilon_r^{GS}{}_{i,j}{}'$:

$$\Delta \varepsilon_{r_{i,j}}{}' = \varepsilon_r^{GS}{}_{i,j}{}' - \overline{\varepsilon_r^{BF}{}_{\cdot,j}{}'}. \qquad (8)$$

From the sample dataset in Figure 10d, the static trend along the rhizotube disappears, and the fluctuating of minima and maxima around zero remained. This approach filters out both the dynamics of the spatially averaged permittivities that are caused by dynamic boundary conditions, as well as the temporally averaged spatial variation of permittivities outside of the growing season that resulted from spatial variations in soil properties and unknown variations in inter-rhizotube distances. In this way, the obtained deviations reflect the dynamic variability in the relative permittivity during the growing season.

6.2 | Results and discussion of time-lapse variability of the GPR data

The approach introduced above to derive the trend-corrected spatial permittivity deviations for the vegetated field $\Delta\varepsilon_{r_{i,j}}{}'$ was applied to Plots 1–3 of R_{UT} and R_{LT} in 2017, and the results are shown in Figure 11. Only days when root information and GPR data were both available were considered. Several different patterns emerge as a function of time, including several consistently increasing maxima
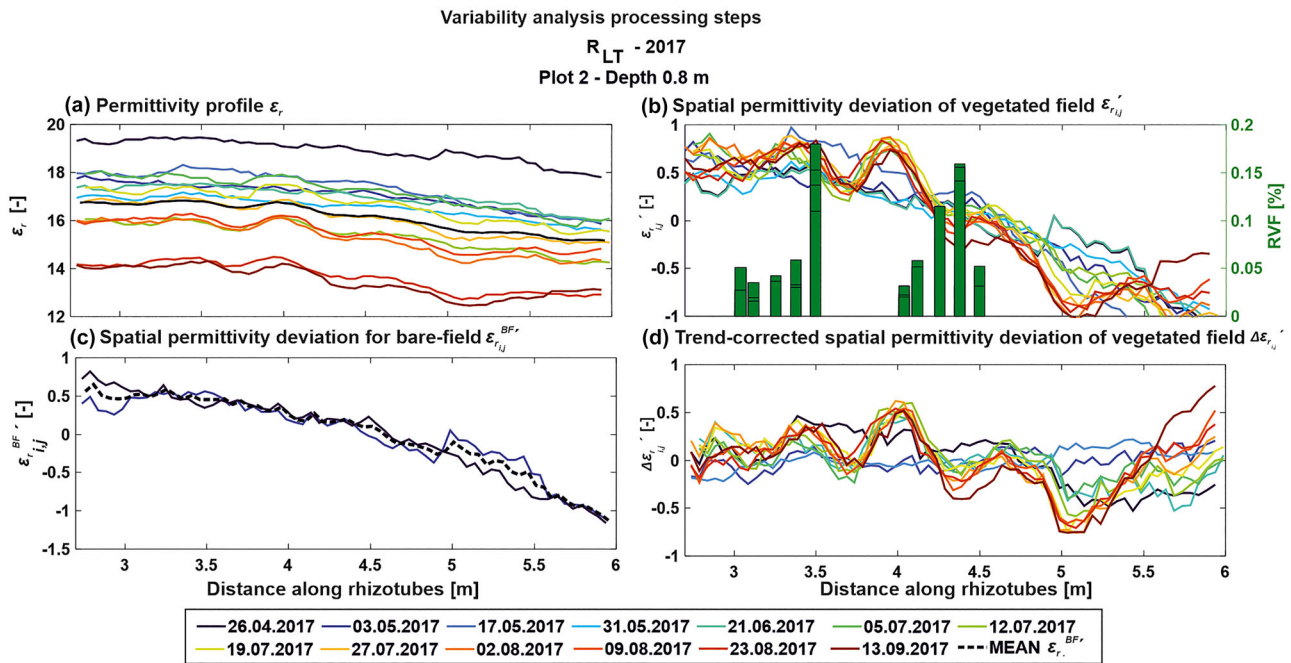
Variability analysis processing steps
R_{LT} - 2017
Plot 2 - Depth 0.8 m

FIGURE 10 Processing steps to derive the trend-corrected spatial permittivity deviation of the vegetated field for R_{LT} Plot 2, depth 0.8 m. The different colors represent the measurement dates. (a) Daily permittivity profile ε_r along the rhizotubes for all dates during the measurement season 2017. (b) Daily spatial permittivity deviation of the vegetated field $\varepsilon_{r_{i,j}}'$. The green bars indicate the root volume fraction (RVF) derived from root images for the different measurement positions. (c) Daily spatial permittivity deviation for the bare-field $\varepsilon_r^{BF}{}_{i,j}'$. The dashed black line represents the mean for 2017. (d) Trend-corrected spatial permittivity deviation of the vegetated field $\Delta\varepsilon_{r_{i,j}}'$.

and minima during the growing season. These patterns were present at the same horizontal location along the rhizotube at different depths and were identified in the $\Delta\varepsilon_{r_{i,j}}'$ data, shown in Figure 11d for Plot 2 in the blue and red frames, respectively. A possible explanation is that the soil water depletion processes had an influence beyond a certain depth range/volume of soil. For R_{UT}, patterns were not as distinct as those for R_{LT}, which had clear maxima and minima along the rhizotube. This could have been caused by fewer roots present in the soil at R_{UT} (see Figure 5a,c,e). For Plot 3, where irrigation was applied, distinctive peaks are apparent along the rhizotubes on certain days, for example, August 9, 2017, and August 23, 2017, between depths of 0.4 and 0.8 m and at a horizontal distance of 2.3–3 m. In both cases, measurements were taken a few days after irrigation was applied (see Tables S1 and S2), and the peaks were probably due to the drip irrigation system which caused spatially variable infiltration.

The same analysis was performed for 2018 and 2020, which can be found in Figures S8 and S9. Evaluating the patterns of $\Delta\varepsilon_{r_{i,j}}'$ for the different crop growing seasons, recurring patterns were observed at some locations (e.g., R_{UT}, Plot 1, depth 0.4 m between 4.5 and 5.5 m; R_{LT}, Plot 2, depth 0.4 and 0.6 m, see Figure 11 and Figure S8). These reoccurring patterns indicate that spatial variations in permittivity likely correspond

with static soil properties that may have influenced water flow and root growth.

6.3 | Probability density function of the trend-corrected permittivity deviation

To quantify the values of $\Delta\varepsilon_{r_{i,j}}'$ in more detail, a normal distribution model was fitted to the data and a range of one standard deviation from the mean (SD) was obtained for the vegetated and BFs. The SD of BF plots was considerably smaller than that of the vegetated field plots (an example of which is shown in Figure 12 for depths 0.2 and 0.6 m, in Plot 2 at R_{UT} and R_{LT}). The presence of the crops clearly increased the permittivity/ $\Delta\varepsilon_{r_{i,j}}'$ variability. When comparing both MR facilities, SD values were generally lower at R_{UT} than at R_{LT}.

By plotting all SD values from 2017 for R_{UT} and R_{LT} for the different depths in Figure 13, low values were observed under BF conditions (non-colored lines), whereas the values for later times initially increased and then decreased. These results indicate that the variability in $\Delta\varepsilon_{r_{i,j}}'$ and therefore SWC, was increasing during the growing season.

A comparison of the different plots for R_{UT} revealed that Plot 1 generally had a higher SD than Plot 2, except for July
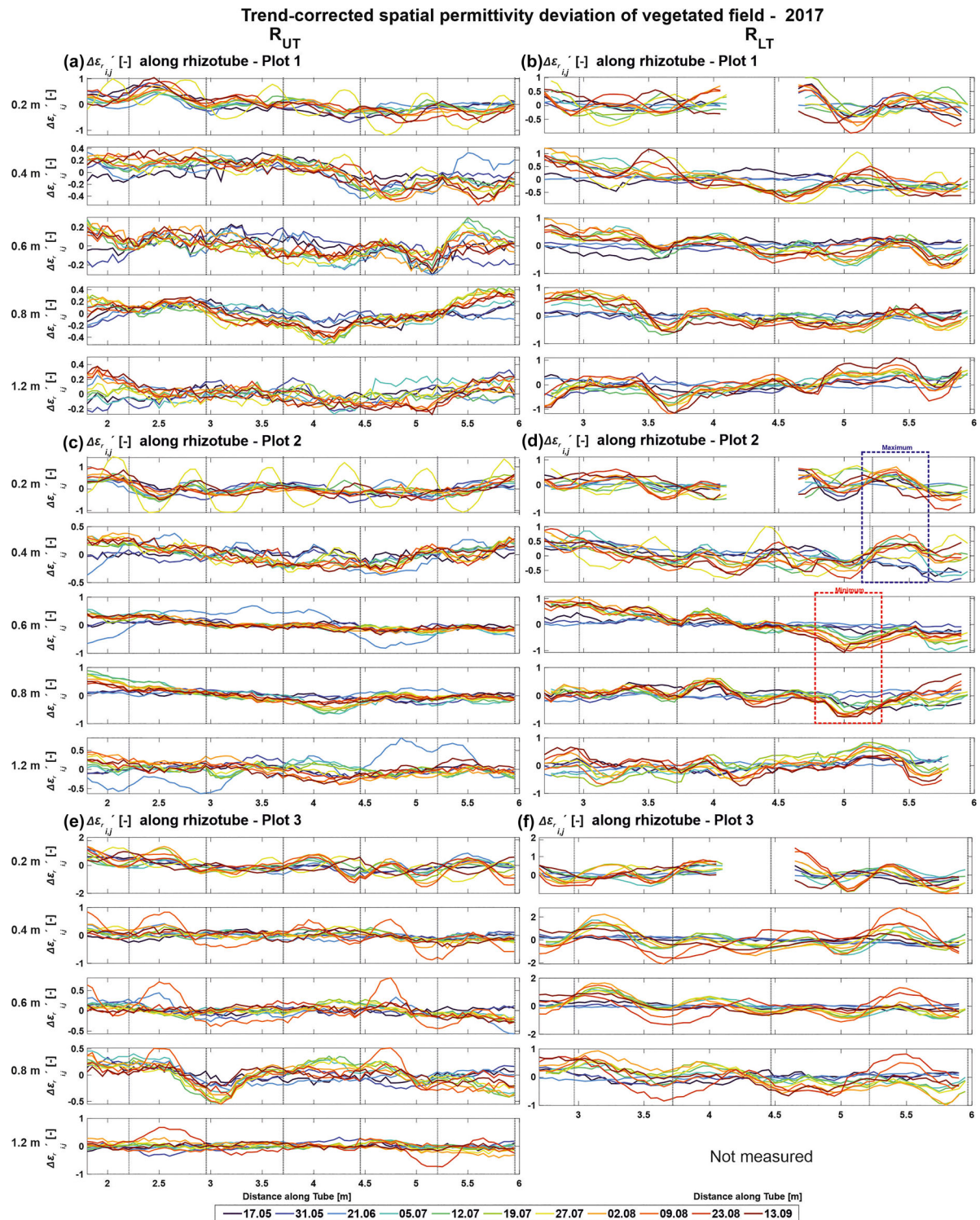
FIGURE 11 Trend-corrected spatial permittivity deviation $\Delta\varepsilon_{r_{i,j}}'$ of the vegetated field, along the rhizotubes over the different plots and depths, for R_{UT} and R_{LT} in 2017. The colored solid lines represent different dates during the crop growing season. The data gap of R_{LT} at 0.2 m depth is caused by the presence of the spectral electrical impedance tomography (sEIT) line.
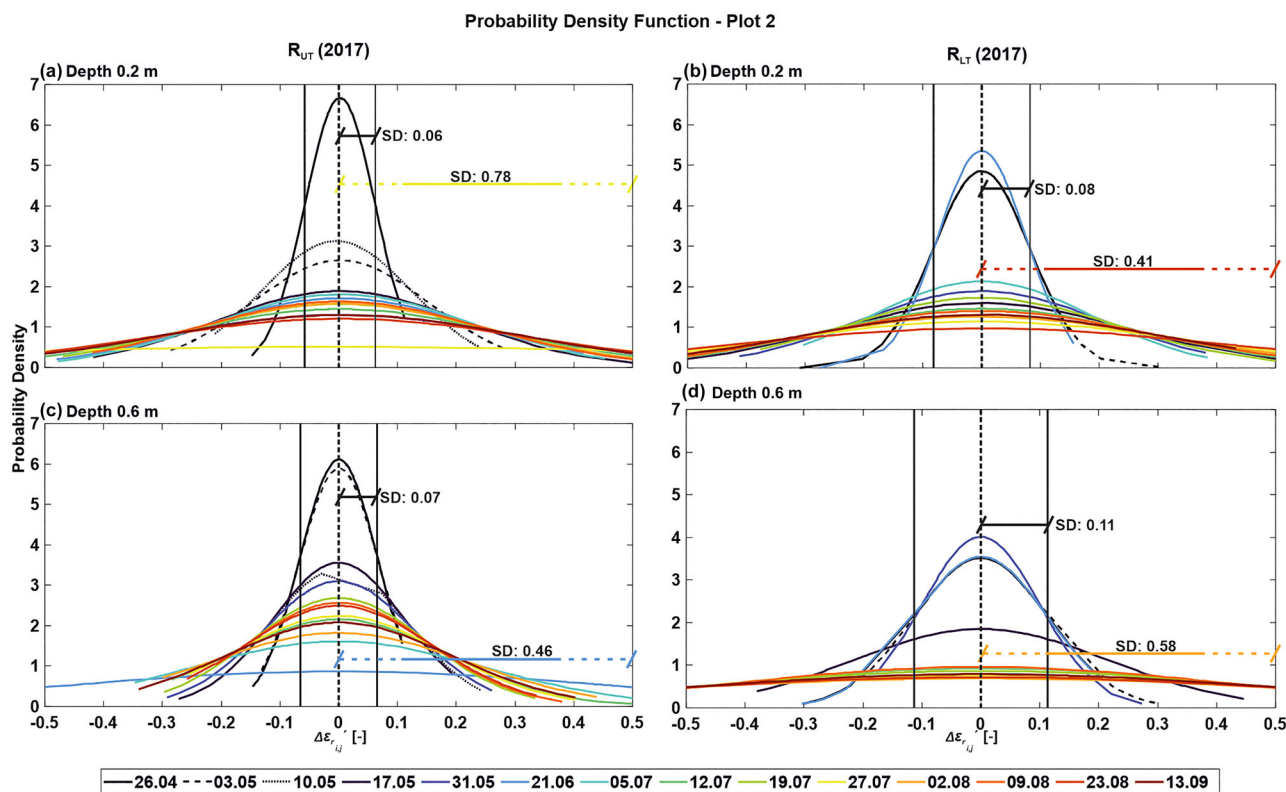
FIGURE 12 Probability density function (PDF) of trend-corrected spatial permittivity deviation $\Delta \varepsilon_{r_{i,j}}'$ for depths of 0.2 m and 0.6 m for Plot 2, for both MR facilities of 2017, respectively. The black solid, dashed, and dotted lines represent the dates for the bare-field measurements, and the colored lines represent the PDF of trend-corrected spatial permittivity deviation $\Delta \varepsilon_{r_{i,j}}'$ for the crop growing season measurements. For PDFs with the most narrow and widest peaks, we added the respective values of the standard deviation (SD).

27, 2017, and that the SD in Plot 1 was at its maximum at a depth of 0.2 m. Plot 3 showed higher SD values than both Plots 1 and 2. For R_{LT}, Plot 3 had the highest SD values, but the difference between Plots 1 and 2 was small.

6.4 | Cross-correlation of depth-dependent RVF and depth-dependent GPR variability

The RVF values in Figure 5 as well as the permittivity variability showed an increase during the growing season. Here, the RVF and SD were cross-correlated individually for every depth as shown in Figure 14. To account for the SD variability in the bare-field conditions present at the MR facilities, the first BF measurement was added to the cross-correlation with an RVF value of 0. Almost all the results from 2017 and 2018 returned a positive correlation, with one exception where the coefficient of determination (R^2) was 0. The remaining cross-correlations resulted in R^2 ranging between 0.02 and 0.9 (Table 3). Out of the 46 cross-correlations, 23 had an $R^2 > 0.5$ ($0.51 < R^2 < 0.9$), and 23 values had an $R^2 < 0.5$ ($0.02 < R^2 < 0.49$). At 0.4-m depth, the correlations are the lowest, and whether this has to do with the interface between the top- and subsoil interface needs to be

investigated. These results indicate that at most depths, the SD, and therefore the permittivity variability, is increasing with increasing RVF. When considered alongside the BF measurements, the presence of roots leads to increased variability in permittivity.

7 | CONCLUSIONS AND OUTLOOK

In this study, root images and time-lapse horizontal crosshole ground penetrating radar (GPR) measurements were made to non-invasively monitor the root zone of maize crops at different depths for different treatments and different soils. Repeated root images and GPR measurements were carried out before and during three separate maize growing seasons. Overall, the analysis of the root images acquired in the upper (R_{UT}) and lower terrace (R_{LT}) MR facilities showed that the root volume fraction (RVF) of the maize crop increased during the crop growing seasons and decreased toward the harvest date. The RVF varied between soil types: in the stoney upper terrace, the roots were not able to reach greater depths due to the stones, whereas the roots were able to grow deeper than the lowest rhizotube in the lower terrace. In addition to soil type, the surface water treatment and previous soil
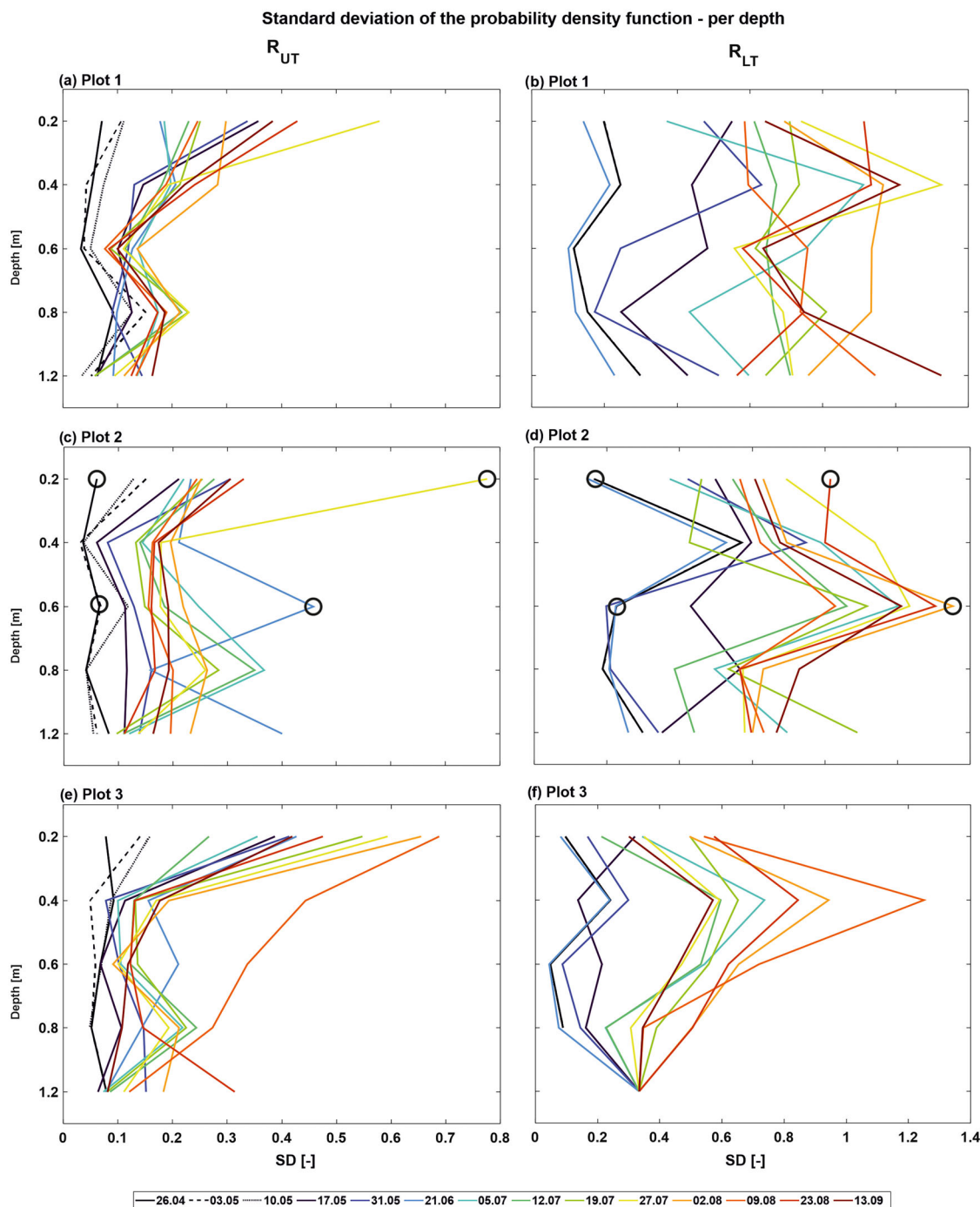
Standard deviation of the probability density function - per depth

FIGURE 13 Standard deviation (SD) values for different depths in 2017 for R_{UT} and R_{LT}, respectively. The black circles indicate the minimum and maximum of the SD, indicated in Figure 12.

management seemed to influence the RVF. It was observed, for instance, that in a plot that was sheltered in previous growing seasons, the maize crops developed more roots than in a plot that was not previously sheltered.

Using the crosshole GPR-derived permittivity values, both the temporal and spatial (vertical and horizontal) permittivity distributions were able to be monitored, and variations for different soil types, weather conditions, and surface water treatments were observed. A direct comparison between the root images and the GPR-derived permittivity values was not possible because of the significant difference in sensing volumes of the two methods (0.21–0.35 cm³ for each GPR-ZOP position and 1.28×10^{-5} cm³ for each set of root images). A time-lapse variability analysis was introduced, where the trend-corrected spatial permittivity deviations were derived for the vegetated field where static influences (soil

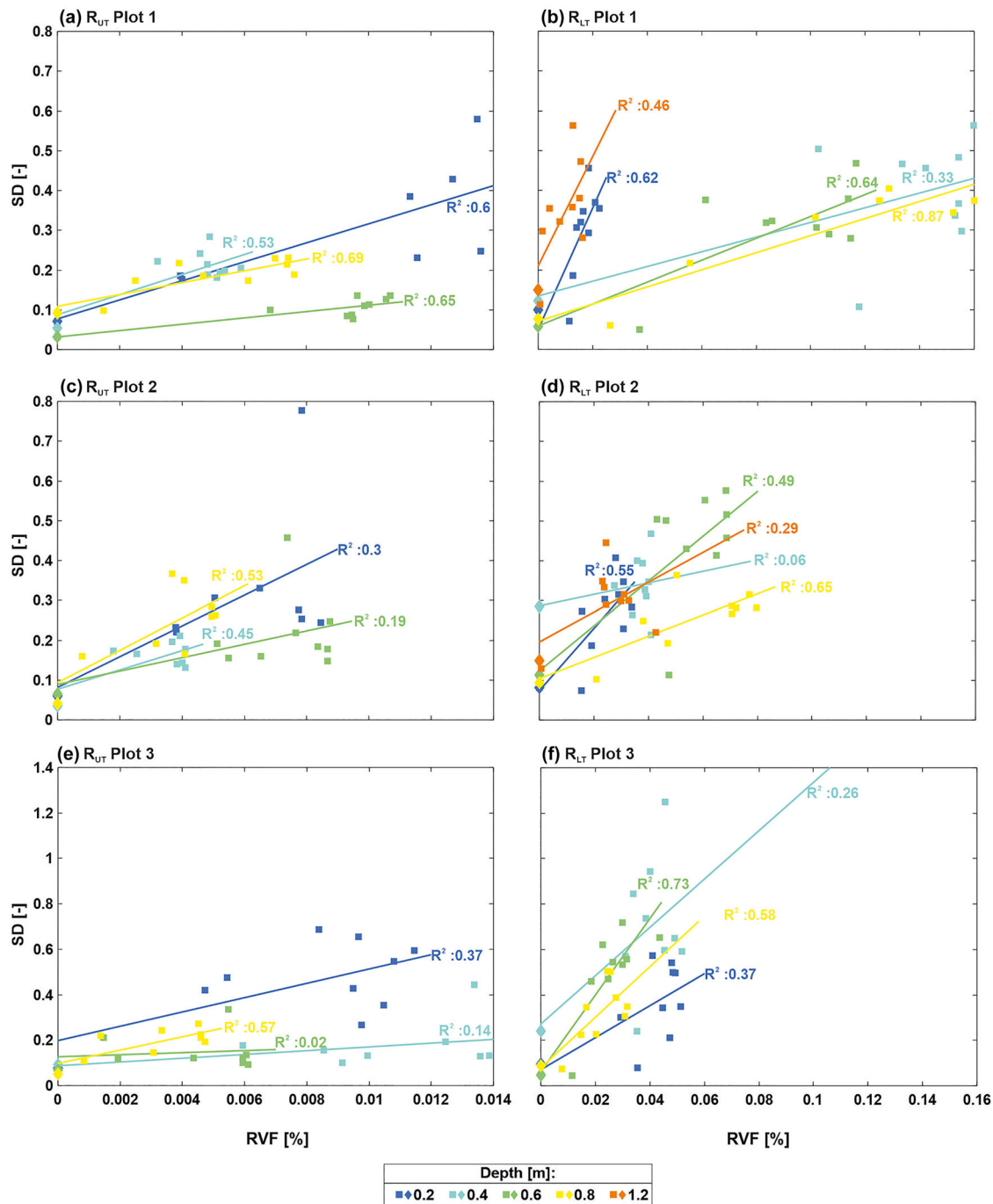**Standard deviation of the probability density function vs. root volume fraction - 2017**

FIGURE 14 Correlation between the root volume fraction (RVF) and the standard deviation (SD) for the individual plots for R_{UT} and R_{LT} in 2017, respectively. The colored squares represent the values for the RVF, and the SD for the vegetated field and the colored diamonds represent the values during bare-field conditions, where the RVF was set to 0. The different colors represent the different depths. The colored lines represent the linear regression per plot and depth, and the R^2 values are indicated next to the regression lines.

heterogeneity or variations in the distance between rhizotubes), as well as dynamic influences (atmospheric conditions), were removed. Next, a probability density function (PDF) model was fit, describing the trend-corrected spatial permittivity deviations for both the vegetated and BFs to obtain a proxy for the permittivity variability. A low stan-

dard deviation, and therefore low permittivity variability, was obtained before and early in the crop growing season, with larger values obtained later in the crop growing season. To investigate the relationship between the trend-corrected spatial permittivity deviations with the RVF in more detail, the PDF standard deviation of the trend-corrected spatial

TABLE 3 Coefficient of determination between the root volume fraction and the SD for R_{UT} and R_{LT} for both years 2017 and 2018.

| | R_{UT} [-] | | | | | | R_{LT} [-] | | | | | |
| | 2017 | | | 2018 | | | 2017 | | | 2018 | | |
Depth (m)	Plot 1	Plot 2	Plot 3	Plot 1	Plot 2	Plot 3	Plot 1	Plot 2	Plot 3	Plot 1	Plot 2	Plot 3
0.2	0.6	0.3	0.37	0.84	0.08	0.56	0.62	0.55	0.37	0.49	0.78	0.72
0.4	0.53	0.45	0.14	0.9	0.07	0.2	0.33	0.06	0.26	0.0	0.13	0.19
0.6	0.65	0.19	0.02	0.07	0.51	0.66	0.64	0.49	0.73	0.48	0.67	0.47
0.8	0.69	0.53	0.57	0.45	0.11	0.86	0.87	0.65	0.58	— [a]	0.34	0.76
1.2	— [a]	— [a]	— [a]	— [a]	— [a]	— [a]	0.46	0.29	— [b]	— [a]	— [a]	— [b]

[a]Three or less data pairs—no cross-correlation was performed.

[b]No GPR measurements were carried out.

permittivity deviations during each season was cross-correlated with the RVF values for each depth, plot, and soil type. Almost all results for 2017 and 2018 were positively correlated, with coefficients of determination ranging between $0.02 < R^2 < 0.9$ (Table 3). Out of the 46 cross-correlations, 23 values had an $R^2 > 0.5$ ($0.51 < R^2 < 0.9$), and 23 values had an $R^2 < 0.5$ ($0.02 < R^2 < 0.49$). These relatively large coefficients of determination show a clear link between RVF and the permittivity variability at multiple soil depths. Additionally, both soil types reacted similarly and provided a comparable number of good correlation pairs, even when within different facilities.

More investigations are necessary to understand why the correlation at some depths is weak. A possible explanation is the difference between the sensing volume (SV) of the GPR measurements and the root image data. The root images represent a significantly smaller 2D space on the rhizotube surface, while the root volume present in the soil volume between the rhizotubes, which is measured by the GPR, remains unknown. Acquiring denser and higher resolution of higher frequency GPR data (between 500 and 1000 MHz) would enhance the imaging of the subsurface between the boreholes. Extending the GPR-zero offset profiling (ZOP) data, with multi-offset GPR data, combined with a ray-based travel time inversion (e.g., Binley et al., 2001; Musil et al., 2006), would also enhance the resolution between the rhizotubes toward 2D and 3D images instead of 1D profiles. These higher resolution images could possibly improve the understanding of processes within the soil–plant continuum and might also allow a more localized correlation. In addition, a possible improvement to the RVF could involve obtaining continuous root images along the entirety of the rhizotubes (as shown in Figure 9). With recent technological developments, measurements along an entire rhizotube can be performed simultaneously, and these RVF data would be expected to better represent the actual RVF changes at different depths and times.

The presented results are based on measurements made during several growing seasons in different soils for different treatments. Taking multiple high-resolution GPR measurements made during the day and night cycle for very hot days and very wet days and analyzing the results with improved imaging approaches would provide additional information. To optimize the monitoring parameters, the construction of a detailed soil–plant–root model that could record time-lapse soil water content changes (depending on the root activity) under changing atmospheric influences would be ideal. In this way, synthetic GPR data could be generated and processed, and the acquisition parameters could be optimized to include as much information as possible to describe the rhizosphere processes that take place under field conditions.

Although the rhizotron facilities provide a great opportunity to deepen the understanding of belowground soil–plant interactions, such facilities are destructive, limited to the plot scale, and are both expensive and time-consuming. Therefore, future challenges will involve finding ways to upscale the link between the permittivity variability and the root image data to surface data. In a next step, combined rhizotube and surface investigations could be analyzed to investigate if a similar link can be observed for aboveground data between root information and GPR data. Furthermore, providing root and plant models with GPR-derived permittivity and hence SWC distribution could help to establish possible surface measurements and to understand the measured signals.

To conclude, this study has established a link between the root volume of maize crops and the spatial variability of horizontal crosshole GPR-derived permittivity values, which is an important step in investigating processes within the soil–plant continuum in more detail. The current approach and the above-described improvements open new possibilities for the combination of non-invasive geophysical measurements with root information measurements to enhance crop models and agricultural management decisions.

AUTHOR CONTRIBUTIONS

Lena Lärm: Conceptualization; data curation; formal analysis; methodology; validation; visualization; writing—original

CONFLICT OF INTEREST STATEMENT

The authors declare no conflicts of interest.

ORCID

Lena Lärm https://orcid.org/0000-0002-0633-4293
Felix Maximilian Bauer https://orcid.org/0000-0002-7441-9897
Jan van der Kruk https://orcid.org/0000-0003-2348-1436
Jan Vanderborght https://orcid.org/0000-0001-7381-3211
Shehan Morandage https://orcid.org/0000-0003-1309-7369
Harry Vereecken https://orcid.org/0000-0002-8051-8517
Andrea Schnepf https://orcid.org/0000-0003-2203-4466
Anja Klotzsche https://orcid.org/0000-0002-7021-5045

REFERENCES

Andrén, O., Rajkai, K., & Kätterer, T. (1991). A non-destructive technique for studies of root distribution in relation to soil moisture. *Agriculture, Ecosystems and Environment*, *34*, 269–278.

Atkinson, J. A., Pound, M. P., Bennett, M. J., & Wells, D. M. (2019). Uncovering the hidden half of plants using new advances in root phenotyping. *Current Opinion in Biotechnology*, *55*, 1–8. https://doi.org/10.1016/j.copbio.2018.06.002

Baroni, G., Ortuani, B., Facchi, A., & Gandolfi, C. (2013). The role of vegetation and soil properties on the spatio-temporal variability of the surface soil moisture in a maize-cropped field. *Journal of Hydrology*, *489*, 148–159. https://doi.org/10.1016/j.jhydrol.2013.03.007

Bauer, F. M., Lärm, L., Morandage, S., Lobet, G., Vanderborght, J., Vereecken, H., & Schnepf, A. (2022). Development and validation of a deep learning based automated minirhizotron image analysis pipeline. *Plant Phenomics*, *2022*, 9758532. https://doi.org/10.34133/2022/9758532

Bauer, J., Weihermüller, L., Huisman, J. A., Herbst, M., Graf, A., Séquaris, J. M., & Vereecken, H. (2011). Inverse determination of heterotrophic soil respiration response to temperature and water content under field conditions. *Biogeochemistry*, *108*, 119–134. https://doi.org/10.1007/s10533-011-9583-1

Binley, A., Winship, P., Middleton, R., Pokar, M., & West, J. (2001). High-resolution characterization of vadose zone dynamics using cross-borehole radar. *Water Resources Research*, *37*, 2639–2652. https://doi.org/10.1029/2000wr000089

Blanchy, G., Watts, C. W., Ashton, R. W., Webster, C. P., Hawkesford, M. J., Whalley, W. R., & Binley, A. (2020). Accounting for heterogeneity in the θ-σ relationship: Application to wheat phenotyping using EMI. *Vadose Zone Journal*, *19*, e20037. https://doi.org/10.1002/vzj2.20037

Blanchy, G., Watts, C. W., Richards, J., Bussell, J., Huntenburg, K., Sparkes, D. L., & Binley, A. (2020). Time-lapse geophysical assessment of agricultural practices on soil moisture dynamics. *Vadose Zone Journal*, *19*, e20080. https://doi.org/10.1002/vzj2.20080

Bogena, H. R., Montzka, C., Huisman, J. A., Graf, A., Schmidt, M., Stockinger, M., & Vereecken, H. (2018). The TERENO-Rur hydrological observatory: A multiscale multi-compartment research platform for the advancement of hydrological science. *Vadose Zone Journal*, *17*, 180055. https://doi.org/10.2136/vzj2018.03.0055

Böhm, W. (1978). Untersuchungen zur Wurzelentwicklung bei Winterweizen. *Zeitschrift für Acker- und Pflanzenbau*, *147*, 264–269.

Brogi, C., Huisman, J. A., Pätzold, S., von Hebel, C., Weihermüller, L., Kaufmann, M. S., & Vereecken, H. (2019). Large-scale soil mapping using multi-configuration EMI and supervised image classification. *Geoderma*, *335*, 133–148. https://doi.org/10.1016/j.geoderma.2018.08.001

Bui, E. N., & Box, J. E. (1992). Stemflow, rain throughfall, and erosion under canopies of corn and Sorghum. *Soil Science Society of America Journal*, *56*, 242–247. https://doi.org/10.2136/sssaj1992.03615995005600010037x

Cai, G., Vanderborght, J., Klotzsche, A., van der Kruk, J., Neumann, J., Hermes, N., & Vereecken, H. (2016). Construction of minirhizotron facilities for investigating root zone processes. *Vadose Zone Journal*, *15*, 1–13. https://doi.org/10.2136/vzj2016.05.0043

Cai, G., Vanderborght, J., Couvreur, V., Mboh, C. M., & Vereecken, H. (2017). Parameterization of root water uptake models considering dynamic root distributions and water uptake compensation. *Vadose Zone Journal*, *17*, 1–21. https://doi.org/10.2136/vzj2016.12.0125

Cai, G., Vanderborght, J., Langensiepen, M., Schnepf, A., Hüging, H., & Vereecken, H. (2018). Root growth, water uptake, and sap flow of winter wheat in response to different soil water conditions. *Hydrology and Earth System Sciences*, *22*, 2449–2470. https://doi.org/10.5194/hess-22-2449-2018

Cassiani, G., Boaga, J., Rossi, M., Putti, M., Fadda, G., Majone, B., & Bellin, A. (2016). Soil–plant interaction monitoring: Small scale example of an apple orchard in Trentino, North-Eastern Italy. *Science of The Total Environment*, *543*, 851–861. https://doi.org/10.1016/j.scitotenv.2015.03.113

Cassidy, N. J. (2009). Electrical and magnetic properties of rocks, soils and fluids. In *Ground penetrating radar theory and applications* (pp. 41–72). Elsevier. https://doi.org/10.1016/b978-0-444-53348-7.00002-8

Cimpoiaşu, M. O., Kuras, O., Pridmore, T., & Mooney, S. J. (2020). Potential of geoelectrical methods to monitor root zone processes and structure: A review. *Geoderma*, *365*, 114232. https://doi.org/10.1016/j.geoderma.2020.114232

Cui, X., Zhang, Z., Guo, L., Liu, X., Quan, Z., Cao, X., & Chen, X. (2021). The root-soil water relationship is spatially anisotropic in shrub-encroached grassland in North China: Evidence from GPR investigation. *Remote Sensing*, *13*, 1137. https://doi.org/10.3390/rs13061137

Delgado, A., Hays, D. B., Bruton, R. K., Ceballos, H., Novo, A., Boi, E., & Selvaraj, M. G. (2017). Ground penetrating radar: A case study for estimating root bulking rate in cassava (*Manihot esculenta* Crantz). *Plant Methods*, *13*, 65. https://doi.org/10.1186/s13007-017-0216-0

do Rosário, G., Oliveira, M., van Noordwijk, M., Gaze, S. R., Brouwer, G., Bona, S., Mosca, G., & Hairiah, K. (2000). Auger sampling, ingrowth cores and pinboard methods. In *Root methods* (pp. 175–210). Springer Berlin Heidelberg. https://doi.org/10.1007/978-3-662-04188-8_6

Ehosioke, S., Nguyen, F., Rao, S., Kremer, T., Placencia-Gomez, E., Huisman, J. A., & Garré, S. (2020). Sensing the electrical properties of roots: A review. *Vadose Zone Journal*, *19*, e20082. https://doi.org/10.1002/vzj2.20082

Galagedara, L. W., Parkin, G. W., Redman, J. D., & Endres, A. L. (2002). Temporal and spatial variation of soil water content measured by borehole GPR under irrigation and drainage. In S. Koppenjan & H. Lee (Eds.), *Proceedings of the Ninth International Conference on Ground Penetrating Radar* (Vol. 4758). Society of Photo-Optical Instrumentation Engineers (SPIE). https://doi.org/10.1117/12.462253

Galagedara, L. W., Parkin, G. W., Redman, J. D., & Endres, A. L. (2003). Assessment of soil moisture content measured by borehole GPR and TDR under transient irrigation and drainage. *Journal of Environmental & Engineering Geophysics*, *8*, 77–86.

Garré, S., Hyndman, D., Mary, B., & Werban, U. (2021). Geophysics conquering new territories: The rise of "agrogeophysics". *Vadose Zone Journal*, *20*, e20115. https://doi.org/10.1002/vzj2.20115

Garré, S., Javaux, M., Vanderborght, J., Pagès, L., & Vereecken, H. (2011). Three-dimensional electrical resistivity tomography to monitor root zone water dynamics. *Vadose Zone Journal*, *10*, 412–424. https://doi.org/10.2136/vzj2010.0079

Garré, S., Pagès, L., Laloy, E., Javaux, M., Vanderborght, J., & Vereecken, H. (2012). Parameterizing a dynamic architectural model of the root system of spring barley from minirhizotron data. *Vadose Zone Journal*, *11*, vzj2011.0179. https://doi.org/10.2136/vzj2011.0179

Guo, D., Li, H., Mitchell, R. J., Han, W., Hendricks, J. J., Fahey, T. J., & Hendrick, R. L. (2007). Fine root heterogeneity by branch order: Exploring the discrepancy in root turnover estimates between minirhizotron and carbon isotopic methods. *New Phytologist*, *177*, 443–456. https://doi.org/10.1111/j.1469-8137.2007.02242.x

Guo, L., Chen, J., Cui, X. H., Fan, B. H., & Lin, H. (2013). Application of ground penetrating radar for coarse root detection and quantification: A review. *Plant and Soil*, *362*, 1–23. https://doi.org/10.1007/s11104-012-1455-5

Hanway, J. J. (1966). *How a corn plant develops* (Special Report no. 38). Iowa State University. https://core.ac.uk/download/pdf/83024409.pdf

Huisman, J. A., Hubbard, S. S., Redman, J. D., & Annan, A. P. (2003). Measuring soil water content with ground penetrating radar. *Vadose Zone Journal*, *2*, 476–491. https://doi.org/10.2136/vzj2018.03.0052

Hupet, F., & Vanclooster, M. (2002). Intraseasonal dynamics of soil moisture variability within a small agricultural maize cropped field. *Journal of Hydrology*, *261*, 86–101. https://doi.org/10.1016/s0022-1694(02)00016-1

Hupet, F., & Vanclooster, M. (2005). Micro-variability of hydrological processes at the maize row scale: Implications for soil water content measurements and evapotranspiration estimates. *Journal of Hydrology*, *303*, 247–270. https://doi.org/10.1016/j.jhydrol.2004.07.017

Jadoon, K. Z., Weihermüller, L., Scharnagl, B., Kowalsky, M. B., Bechtold, M., Hubbard, S. S., & Lambot, S. (2012). Estimation of soil hydraulic parameters in the field by integrated hydrogeophysical inversion of time-lapse ground-penetrating radar data. *Vadose Zone Journal*, *11*, vzj2011.0177.

Johnson, M. G., Tingey, D. T., Phillips, D. L., & Storm, M. J. (2001). Advancing fine root research with minirhizotrons. *Environmental and Experimental Botany*, *45*, 263–289. https://doi.org/10.1016/s0098-8472(01)00077-6

Jol, H. M. (2009). Ground penetrating radar theory and applications. Elsevier Science. https://doi.org/10.1016/B978-0-444-53348-7.X0001-4

Klotzsche, A., van der Kruk, J., He, G., & Vereecken, H. (2016). GPR full-waveform inversion of horizontal ZOP borehole data using GprMax. *Proceedings of the 16th International Conference on Ground Penetrating Radar, GPR*, 16321910. https://doi.org/10.1109/ICGPR.2016.7572695

Klotzsche, A., Jonard, F., Looms, M. C., van der Kruk, J., & Huisman, J. A. (2018). Measuring soil water content with ground penetrating radar: A decade of progress. *Vadose Zone Journal*, *17*, 180052. https://doi.org/10.2136/vzj2018.03.0052

Klotzsche, A., Lärm, L., Vanderborght, J., Cai, G., Morandage, S., Zörner, M., & Kruk, J. (2019). Monitoring soil watercontent using time-lapse horizontal borehole GPR data at the field-plot scale. *Vadose Zone Journal*, *18*, 190044. https://doi.org/10.2136/vzj2019.05.0044

Klotzsche, A., Vereecken, H., & van der Kruk, J. (2019). Review of crosshole ground-penetrating radar full-waveform inversion of experimental data: Recent developments, challenges, and pitfalls. *Geophysics*, *84*, H13–H28. https://doi.org/10.1190/geo2018-0597.1

Lärm, L., Bauer, F. M., Hermes, N., van der Kruk, J., Vereecken, H., Vanderborght, J., & Klotzsche, A. (2023). Multi-year belowground data of minirhizotron facilities in Selhausen. *Scientific Data*, *10*, 672. https://doi.org/10.1038/s41597-023-02570-9

Liu, X., Chen, J., Butnor, J. R., Qin, G., Cui, X., Fan, B., & Guo, L. (2020). Noninvasive 2D and 3D mapping of root zone soil moisture through the detection of coarse roots with ground-penetrating radar. *Water Resources Research*, *56*, e2019WR026930. https://doi.org/10.1029/2019wr026930

Liu, X., Cui, X., Guo, L., Chen, J., Li, W., Yang, D., & Lin, H. (2019). Non-invasive estimation of root zone soil moisture from coarse root reflections in ground-penetrating radar images. *Plant and Soil*, *436*, 623–639. https://doi.org/10.1007/s11104-018-03919-5

Liu, X., Dong, X., Xue, Q., Leskovar, D. I., Jifon, J., Butnor, J. R., & Marek, T. (2017). Ground penetrating radar (GPR) detects fine roots

of agricultural crops in the field. *Plant and Soil*, *423*, 517–531. https://doi.org/10.1007/s11104-017-3531-3

Maeght, J.-L., Rewald, B., & Pierret, A. (2013). How to study deep roots—And why it matters. *Frontiers in Plant Science*, *4*, 299. https://doi.org/10.3389/fpls.2013.00299

Morandage, S., Vanderborght, J., Zörner, M., Cai, G., Leitner, D., Vereecken, H., & Schnepf, A. (2021). Root architecture development in stony soils. *Vadose Zone Journal*, *20*, e20133. https://doi.org/10.1002/vzj2.20133

Musil, M., Maurer, H., Hollinger, K., & Green, A. G. (2006). Internal structure of an alpine rock glacier based on crosshole georadar traveltimes and amplitudes. *Geophysical Prospecting*, *54*, 273–285. https://doi.org/10.1111/j.1365-2478.2006.00534.x

Nguyen, T. H., Langensiepen, M., Gaiser, T., Webber, H., Ahrends, H., Hueging, H., & Ewert, F. (2022). Responses of winter wheat and maize to varying soil moisture: From leaf to canopy. *Agricultural and Forest Meteorology*, *314*, 108803. https://doi.org/10.1016/j.agrformet.2021.108803

Parsekian, A. D., Slater, L., & Schäfer, K. V. (2012). Small root biomass effect on the dielectric properties of soil. *Vadose Zone Journal*, *11*. https://doi.org/10.2136/vzj2011.0049

Rewald, B., & Ephrath, J. E. (2013). Minirhizotron techniques. In *Plant roots* (pp. 735–750). CRC Press.

Rodríguez-Robles, U., Arredondo, T., Huber-Sannwald, E., Ramos-Leal, J. A., & Yépez, E. A. (2017). Technical note: Application of geophysical tools for tree root studies in forest ecosystems in complex soils. *Biogeosciences*, *14*, 5343–5357. https://doi.org/10.5194/bg-14-5343-2017

Schlüter, S., Vogel, H.-J., Ippisch, O., & Vanderborght, J. (2013). Combined impact of soil heterogeneity and vegetation type on the annual water balance at the field scale. *Vadose Zone Journal*, *12*, vzj2013.03.0053. https://doi.org/10.2136/vzj2013.03.0053

Schmäck, J., Weihermüller, L., Klotzsche, A., Hebel, C., Pätzold, S., Welp, G., & Vereecken, H. (2021). Large-scale detection and quantification of harmful soil compaction in a post-mining landscape using multi-configuration electromagnetic induction. *Soil Use and Management*, *38*, 212–228. https://doi.org/10.1111/sum.12763

Seethepalli, A., Dhakal, K., Griffiths, M., Guo, H., Freschet, G. T., & York, L. M. (2021). RhizoVision Explorer: Open-source software for root image analysis and measurement standardization. *AoB Plants*, *13*, plab056. https://doi.org/10.1093/aobpla/plab056

Shanahan, P. W., Binley, A., Whalley, W. R., & Watts, C. W. (2015). The use of electromagnetic induction to monitor changes in soil moisture profiles beneath different wheat genotypes. *Soil Science Society of America Journal*, *79*, 459–466. https://doi.org/10.2136/sssaj2014.09.0360

Smith, A. G., Han, E., Petersen, J., Olsen, N. A., Giese, C., Athmann, M., & Thorup-Kristensen, K. (2022). RootPainter: Deep learning segmentation of biological images with corrective annotation. *New Phytologist*, *236*, 774–791. https://doi.org/10.1111/nph.18387

Steelman, C. M., & Endres, A. L. (2011). Comparison of petrophysical relationships for soil moisture estimation using GPR ground waves. *Vadose Zone Journal*, *10*, 270–285. https://doi.org/10.2136/vzj2010.0040

Svane, S. F., Jensen, C. S., & Thorup-Kristensen, K. (2019). Construction of a large-scale semi-field facility to study genotypic differences in deep root growth and resources acquisition. *Plant Methods*, *15*, 26. https://doi.org/10.1186/s13007-019-0409-9

Trachsel, S., Kaeppler, S. M., Brown, K. M., & Lynch, J. P. (2010). Shovelomics: High throughput phenotyping of maize (*Zea mays* L.) root architecture in the field. *Plant and Soil*, *341*, 75–87. https://doi.org/10.1007/s11104-010-0623-8

Vamerali, T., Bandiera, M., & Mosca, G. (2011). Minirhizotrons in modern root studies. In *Measuring roots* (pp. 341–361). Springer Berlin Heidelberg. https://doi.org/10.1007/978-3-642-22067-8_17

van Noordwijk, M., Brouwer, G., Meijboom, F., do Rosário, G., Oliveira, M., & Bengough, A. G. (2001). Trench profile techniques and core break methods. In *Root methods* (pp. 211–233). Springer Berlin Heidelberg. https://doi.org/10.1007/978-3-662-04188-8_7

Wasson, A., Bischof, L., Zwart, A., & Watt, M. (2016). A portable fluorescence spectroscopy imaging system for automated root phenotyping in soil cores in the field. *Journal of Experimental Botany*, *67*, 1033–1043. https://doi.org/10.1093/jxb/erv570

Weaver, J. E. (1926). *Root development of field crops*. McGraw-Hill.

Weigand, M., & Kemna, A. (2017). Multi-frequency electrical impedance tomography as a non-invasive tool to characterize and monitor crop root systems. *Biogeosciences*, *14*, 921–939. https://doi.org/10.5194/bg-14-921-2017

Weigand, M., & Kemna, A. (2018). Imaging and functional characterization of crop root systems using spectroscopic electrical impedance measurements. *Plant and Soil*, *435*, 201–224. https://doi.org/10.1007/s11104-018-3867-3

Weigand, M., Zimmermann, E., Michels, V., Huisman, J. A., & Kemna, A. (2022). Design and operation of a long-term monitoring system for spectral electrical impedance tomography (sEIT). *Geoscientific Instrumentation, Methods and Data Systems*, *11*, 413–433. https://doi.org/10.5194/gi-11-413-2022

Weihermüller, L., Huisman, J. A., Lambot, S., Herbst, M., & Vereecken, H. (2007). Mapping the spatial variation of soil water content at the field scale with different ground penetrating radar techniques. *Journal of Hydrology*, *340*, 205–216. https://doi.org/10.1016/j.jhydrol.2007.04.013

Whalley, W. R., Binley, A., Watts, C. W., Shanahan, P., Dodd, I. C., Ober, E. S., & Hawkesford, M. J. (2017). Methods to estimate changes in soil water for phenotyping root activity in the field. *Plant and Soil*, *415*, 407–422. https://doi.org/10.1007/s11104-016-3161-1

Wijewardana, Y. G., & Galagedara, L. W. (2010). Estimation of spatio-temporal variability of soil water content in agricultural fields with ground penetrating radar. *Journal of Hydrology*, *391*, 26–35. https://doi.org/10.1016/j.jhydrol.2010.06.036

Yu, Y., Klotzsche, A., Weihermüller, L., Huisman, J. A., Vanderborght, J., Vereecken, H., & der Kruk, J. (2020). Measuring vertical soil water content profiles by combining horizontal borehole and dispersive surface ground penetrating radar data. *Near Surface Geophysics*, *18*, 275–294. https://doi.org/10.1002/nsg.12099

Yu, Y., Weihermüller, L., Klotzsche, A., Lärm, L., Vereecken, H., & Huisman, J. A. (2021). Sequential and coupled inversion of horizontal borehole ground penetrating radar data to estimate soil hydraulic properties at the field scale. *Journal of Hydrology*, *596*, 126010. https://doi.org/10.1016/j.jhydrol.2021.126010

SUPPORTING INFORMATION

Additional supporting information can be found online in the Supporting Information section at the end of this article.

APPENDIX

DAILY SPATIAL PERMITTIVITY DEVIATION FOR THE BARE-FIELD

The results of the spatial permittivity deviation of the bare-field $\varepsilon_{r}^{\mathrm{BF}}{}'_{i,j}$ for 2017 and 2018 indicated that the 2 years showed similar values along the rhizotubes for the different plots and depths with similar patterns for both sites. Since no crops were present for these measurements, these daily variabilities along the rhizotubes could be linked to the static factors of soil heterogeneity and rhizotube deviation. Comparing all depths for all three plots in R_{UT}, minima and maxima in i along the rhizotubes were identified. These were more distinct, and the variation between the individual measurement seasons was less significant in comparison with R_{LT}. In contrast, R_{LT} did not show these clear minima and maxima in $\varepsilon_{r}^{\mathrm{BF}}{}'_{i,j}$. In fact, only at depths of 0.2 and 0.4 m, changes on the extent of $\varepsilon_{r}^{\mathrm{BF}}{}'_{i,j}$ along the rhizotubes were recognizable. For greater depths, we could see trends along the rhizotubes where $\varepsilon_{r}^{\mathrm{BF}}{}'_{i,j}$ was either steadily increasing (e.g., Plot 3 at a depth of 0.8 m) or steadily decreasing (e.g., Plot 2 at a depth of 0.8 m) along the rhizotubes. Additionally, the variation between the individual measurement seasons was larger for R_{LT} compared to R_{UT}.

Daily spatial permittivity deviation for the bare-field
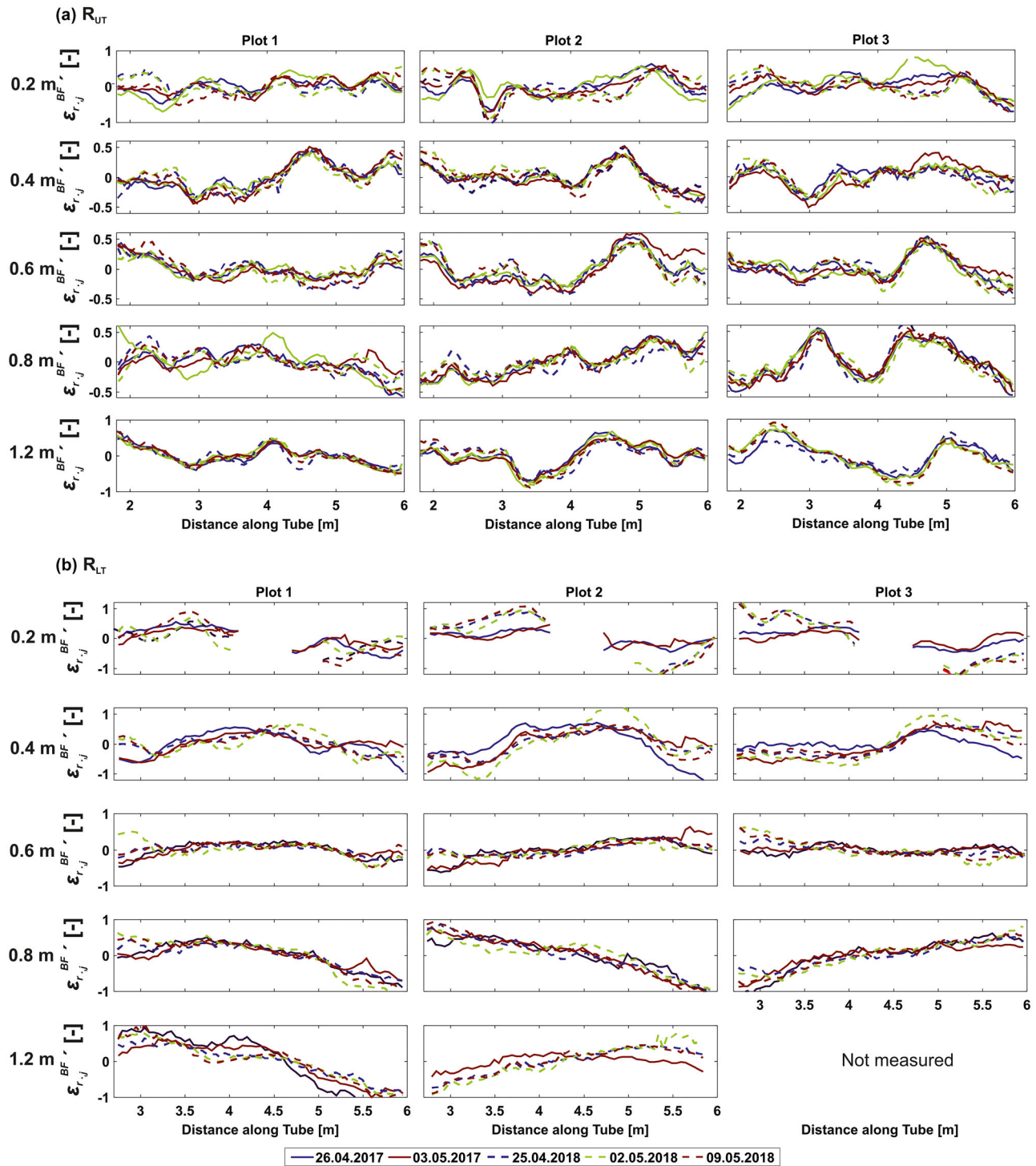

FIGURE A1 Daily spatial permittivity deviation for the bare-field $\varepsilon_{r\ i,j}^{\mathrm{BF}}{}'$ along the rhizotubes under bare-field conditions for (a) R_{UT} and (b) R_{LT} for the crop growing seasons 2017 and 2018. The colored solid lines indicate the daily spatial permittivity deviation for the bare-field $\varepsilon_{r\ i,j}^{\mathrm{BF}}{}'$ values of 2017, and the colored dashed lines indicate the daily spatial permittivity deviation for the bare-field $\varepsilon_{r\ i,j}^{\mathrm{BF}}{}'$ of 2018.
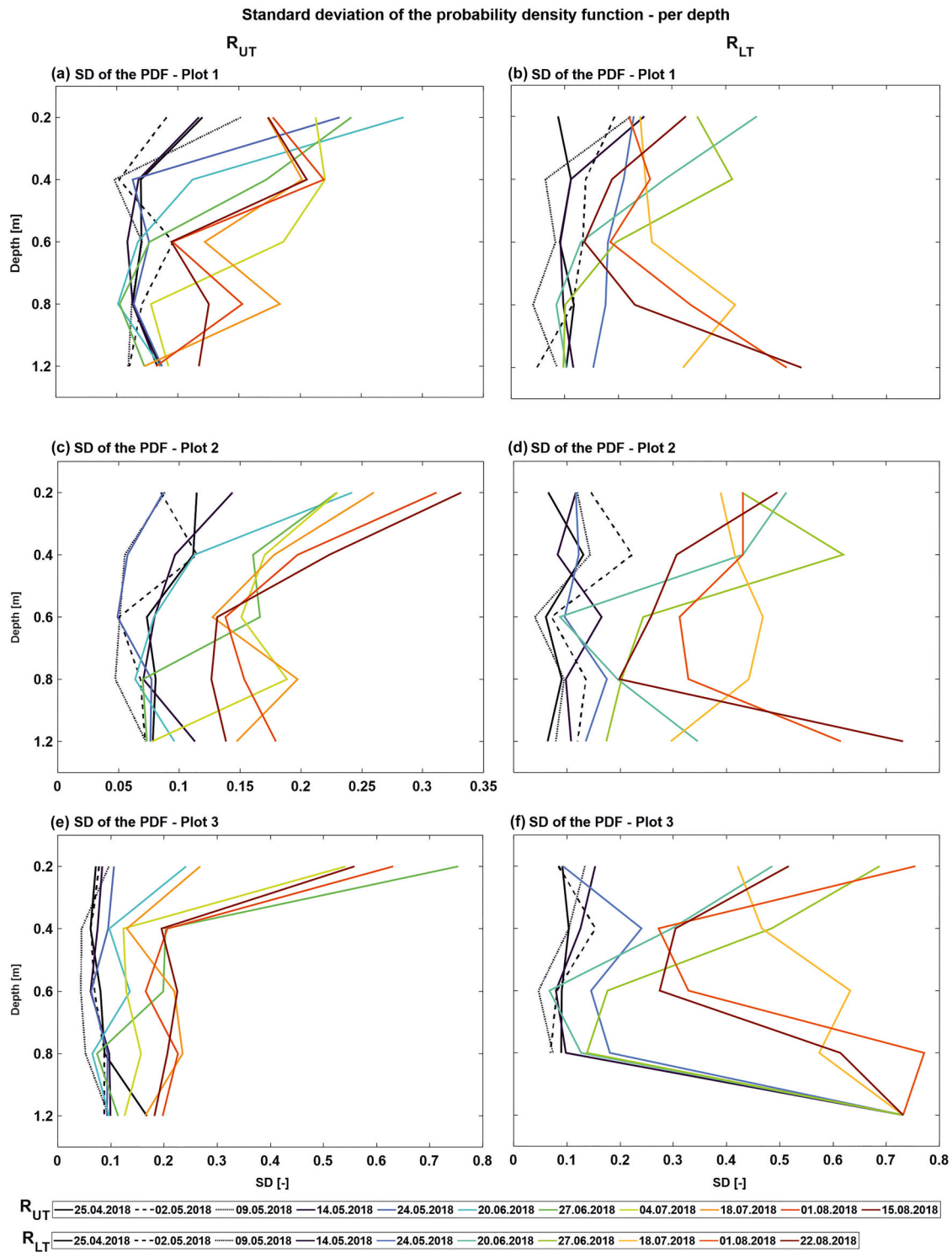
FIGURE A2.1 Standard deviation (SD) values for different depths in 2018 for R_{UT} and R_{LT}, respectively. Note that the axes limits differ between the different depths to show the SD variations between the individual depths.

Standard deviation of the probability density function vs. root volume fraction - 2018
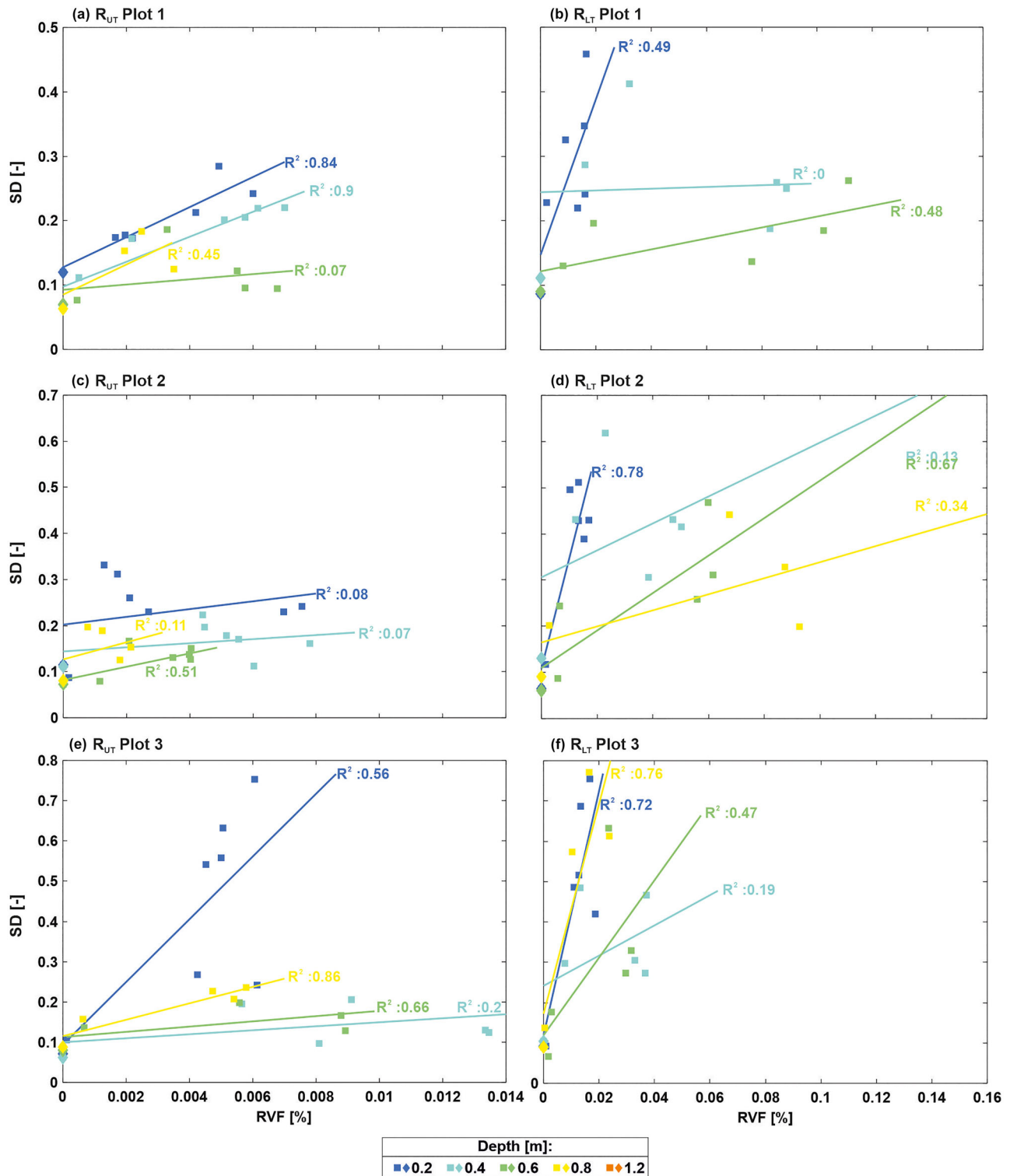

FIGURE A2.2 Correlation between the root volume fraction (RVF) and the SD for the individual plots for R_{UT} and R_{LT} in 2018, respectively. The colored squares represent the values for the RVF and the SD for the vegetated field and the colored diamonds represent the values during the bare-field, where the RVF was set to 0. The different colors represent the different depths. The colored lines represent the linear regression per plot and depth, the R^2 values are indicated next to the regression lines.